

Leaky Slope Waves and Sea Level: Unusual Consequences of the Beta Effect along Western Boundaries with Bottom Topography and Dissipation

ANTHONY WISE

National Oceanography Centre, and Department of Earth, Ocean and Ecological Sciences, University of Liverpool, Liverpool, United Kingdom

CHRIS W. HUGHES

Department of Earth, Ocean and Ecological Sciences, University of Liverpool, and National Oceanography Centre, Liverpool, United Kingdom

JEFF A. POLTON AND JOHN M. HUTHNANCE

National Oceanography Centre, Liverpool, United Kingdom

(Manuscript received 5 April 2019, in final form 29 October 2019)


ABSTRACT

Coastal trapped waves (CTWs) carry the ocean's response to changes in forcing along boundaries and are important mechanisms in the context of coastal sea level and the meridional overturning circulation. Motivated by the western boundary response to high-latitude and open-ocean variability, we use a linear, barotropic model to investigate how the latitude dependence of the Coriolis parameter (β effect), bottom topography, and bottom friction modify the evolution of western boundary CTWs and sea level. For annual and longer period waves, the boundary response is characterized by modified shelf waves and a new class of leaky slope waves that propagate alongshore, typically at an order slower than shelf waves, and radiate short Rossby waves into the interior. Energy is not only transmitted equatorward along the slope, but also eastward into the interior, leading to the dissipation of energy locally and offshore. The β effect and friction result in shelf and slope waves that decay alongshore in the direction of the equator, decreasing the extent to which high-latitude variability affects lower latitudes and increasing the penetration of open-ocean variability onto the shelf—narrower continental shelves and larger friction coefficients increase this penetration. The theory is compared with observations of sea level along the North American east coast and qualitatively reproduces the southward displacement and amplitude attenuation of coastal sea level relative to the open ocean. The implications are that the β effect, topography, and friction are important in determining where along the coast sea level variability hot spots occur.

1. Introduction

The propagation of waves along ocean boundaries occurs as part of the oceanic adjustment to variability in environmental forcing, such as wind stress or buoyancy. Over a period of time, wave propagation enables changes in forcing to be communicated over large distances along boundaries and between the open ocean and coast. The characteristics of these waves, often referred to as coastal trapped waves (CTWs) because of their decaying away

from the boundary, are therefore important to oceanic adjustment processes—for instance, regional sea level (Hughes and Meredith 2006) and the meridional overturning circulation (Roussenov et al. 2008; Buckley and Marshall 2016). CTWs are important to the transmission of energy along boundaries and are relevant in the context of energy dissipation at western boundaries and the oceanic energy budget—for example, as a sink of ocean-eddy energy (Zhai et al. 2010). An improved understanding of the physics at boundaries is also recognized as desirable to improve the dynamical justification

 Denotes content that is immediately available upon publication as open access.

Corresponding author: Anthony Wise, anwise@noc.ac.uk



This article is licensed under a [Creative Commons Attribution 4.0 license](http://creativecommons.org/licenses/by/4.0/) (<http://creativecommons.org/licenses/by/4.0/>).

DOI: 10.1175/JPO-D-19-0084.1

© 2020 American Meteorological Society

for subgrid-scale parameterizations in ocean circulation models (OCMs) (Deremble et al. 2017), which can have significant effects on important oceanic features such as Gulf Stream separation sensitivity to viscosity parameterization (Bryan et al. 2007).

At ocean boundaries, where the no normal flow condition holds, variability in the open (interior) ocean or at higher (poleward) latitudes results in an adjustment of potential vorticity that manifests as waves propagating along the boundary. The properties of these waves have been explored in idealized settings for different boundary geometries (vertical sidewall; sloping sidewalls), stratification profiles, and frequencies (see Mysak 1980; Huthnance et al. 1986; Hughes et al. 2019). In the following we restrict ourselves to variability at subinertial frequencies, $\omega < f$, where f is the Coriolis parameter.

For vertical-sidewall boundaries, CTWs are typically a series of barotropic and baroclinic Kelvin waves propagating cyclonically around the ocean (boundary on the right in the Northern Hemisphere). With the inclusion of sloping sidewalls at the boundary, the modal structure ceases to be separable in the horizontal and vertical. In the barotropic limit, the modes evolve into shelf waves.

Wajswowicz and Gill (1986) showed friction to attenuate Kelvin waves resulting in the decay of alongshore amplitude. Brink and Allen (1978) applied bottom friction to a barotropic model with a continental shelf and slope and found the wave response to local alongshore forcing to be damped and with a cross-shore phase lag. The amplitude of this boundary response is associated with the energy flux at the boundary and is relevant to energy dissipation and monitoring of the meridional overturning circulation, as discussed in Kanzow et al. (2009) and Marshall and Johnson (2013). Friction has also been shown to promote the interior ocean contribution to western boundary coastal sea level (Minobe et al. 2017; Wise et al. 2018).

The theory of CTWs is based primarily on the assumption that the Coriolis parameter is constant (f -plane approximation), particularly for sloping sidewalls. However, Miles (1972) found that the curvature of Earth and changes in depth over a continental shelf modify wave amplitude and phase speed at inertial frequencies ($\omega \approx f$) (he used an inviscid barotropic model). He also showed the wave amplitude to decay with latitude, proportionally to $f^{1/2}$, a result previously obtained by Moore (1968) for equatorial Kelvin waves. Johnson and Marshall (2002) identified the attenuated Kelvin wave amplitude at western boundaries as a key component in an “equatorial buffer” mechanism to describe the transmission of thermohaline variability around the Atlantic, with information transmitted westward from the eastern boundary as long Rossby

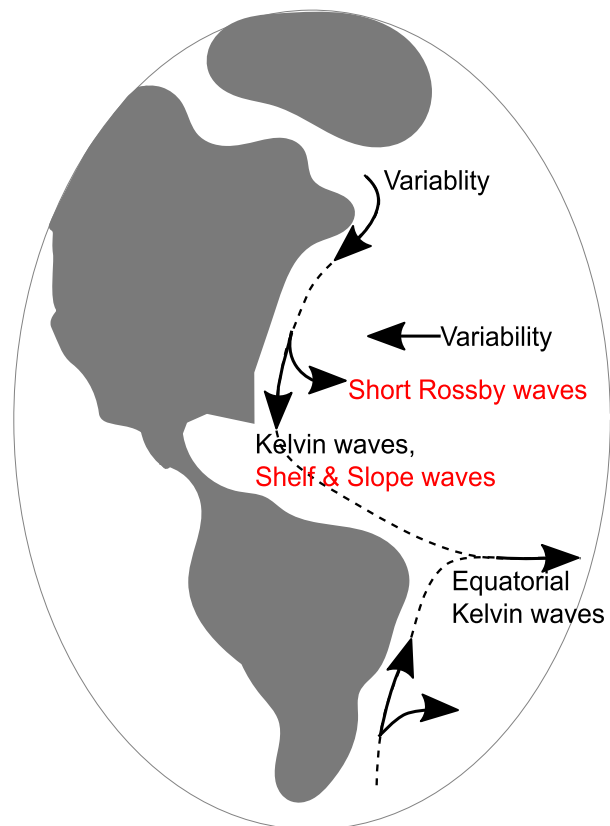


FIG. 1. Schematic of the transmission of variability along western boundaries and eastward at the equator. The shelf, slope, and short Rossby waves (denoted in red) are the subject of this study.

waves, equatorward along the western boundary and eastward at the equator. Allen and Romea (1980) also showed that equatorial baroclinic disturbances could be carried poleward along eastern boundaries as Kelvin waves that change into barotropic shelf waves at midlatitudes. Figure 1 illustrates the relevant western boundary information pathways, with red denoting the wave types that are the subject of this study.

Using a frictional reduced-gravity model, Marshall and Johnson (2013) extended the vertical-sidewall, β -plane theory to wave periods longer than a few months and found that buoyancy anomalies could propagate along western and eastern boundaries as short and long Rossby waves, respectively. They found the western boundary wave to dissipate virtually all its energy during propagation toward the equator, with no dependence on the value of the dissipation coefficient.

While Marshall and Johnson (2013) demonstrated the importance of the β effect and friction at western boundaries, they noted that the inclusion of more realistic bottom topography would modify the results. It is our intention with this paper to use a simple model

to extend their investigation of the western boundary response to the case in which the bottom topography includes a continental shelf and slope. As we will see, the boundary response is dependent on the evolution of CTWs that are lost in the vertical-sidewall assumption—and the β effect and friction have interesting effects on their behavior, including the addition of a new class of leaky slope wave.

The paper is structured as follows. In section 2 we formulate the problem and present wave solutions. In section 3 we discuss the cross-shore structure of these waves. Section 4 discusses the alongshore evolution and energetics of waves excited by high-latitude forcing, and section 5 continues this for forcing from the interior. Section 6 applies the results to western boundary sea level, and we conclude with implications and a summary of the key points.

2. Formulation and solutions

We will be considering throughout a rectangular section of the ocean between a high and low latitude boundary (not reaching the equator) that stretches from a western boundary coastline to a boundary $O(100)$ km offshore. For a coordinate system with x in the zonal and y in the meridional direction, we consider a straight western boundary coastline, oriented along the y axis (meridionally) at $x = 0$, with the equator at $y = 0$ and larger y corresponding to higher latitudes. Bottom topography h is taken to be uniform alongshore, that is, independent of y , but variable in the cross-shore direction, that is, $h = h(x)$. Figure 2a gives a schematic of the bottom topography with $x = x_s$ denoting the shelf break, $x = x_b$ the bottom of the slope, and $x = x_{in}$ the boundary with the interior. Note that the boundary forcing (applied at the boundary with the interior) is applied east of where the boundary response has decayed. Depth at the shelf break and bottom of the slope are denoted by H_s and H_b . We assume that depth tends to zero at the coast and increases

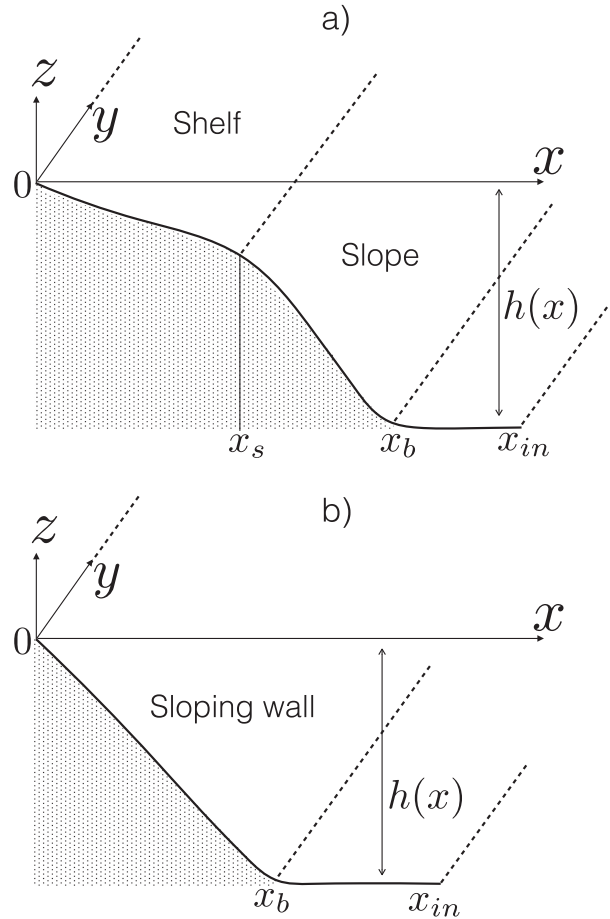


FIG. 2. Schematic illustrating the coordinates and bottom topography for (a) a continental shelf and slope and (b) a sloping sidewall. The shelf break, slope bottom, and boundary with the interior ocean are denoted by x_s , x_b , and x_{in} , respectively.

monotonically away from the coast. For numerical calculations we use fifth-order smoother-step functions to define the shelf, slope and offshore portions of $h(x)$; that is,

$$h(x) = \begin{cases} H_s \left[6 \left(\frac{x}{x_s} \right)^5 - 15 \left(\frac{x}{x_s} \right)^4 + 10 \left(\frac{x}{x_s} \right)^3 \right] & \text{for } 0 \leq x \leq x_s \\ H_s + (H_b - H_s) \left[6 \left(\frac{x - x_s}{x_b - x_s} \right)^5 - 15 \left(\frac{x - x_s}{x_b - x_s} \right)^4 + 10 \left(\frac{x - x_s}{x_b - x_s} \right)^3 \right] & \text{for } x_s < x \leq x_b \end{cases}, \quad (1)$$

with $h(x) \approx H_b$ east of the slope ($x > x_b$).

In the following we consider solutions of the linearized, depth-integrated shallow water equations for annual-to-decadal variability ($\omega \ll f$). The equatorial

β -plane Coriolis parameter, $f = \beta y$, is used for simplicity—the solution method is valid for a general $f(y)$, however. Assuming the flow to be bathymetrically steered alongshore and with $\omega/f \ll 1$, we follow

Gill and Schumann (1974) (long-wave approximation) and allow the zonal momentum equation to be in geostrophic balance while retaining the (linear) bottom friction [as in Csanady (1978)] in the meridional momentum equation,

$$-f\eta v + gh \frac{\partial \tilde{\eta}}{\partial x} = 0 \quad \text{and} \quad (2)$$

$$h \frac{\partial v}{\partial t} + fhu + gh \frac{\partial \tilde{\eta}}{\partial y} = -rv, \quad (3)$$

with $\mathbf{u} = (u, v)$ being the velocity, $\tilde{\eta} = \tilde{\eta}(x, y, t)$ being the inverse barometer corrected dynamic topography (dynamic sea level), g being gravity, and r being the linear friction parameter. For the continuity equation

$$\frac{\partial \tilde{\eta}}{\partial t} + \frac{\partial(uh)}{\partial x} + \frac{\partial(vh)}{\partial y} = 0, \quad (4)$$

we begin by retaining the free-surface for discussion but we ultimately follow Buchwald and Adams (1968) and Gill and Schumann (1974) in making the rigid-lid approximation such that the continuity equation becomes $\nabla \cdot (\mathbf{u}h) = 0$.

Taking the vertical component of the curl of the momentum equations, (2)/ h and (3)/ h , and substituting in the continuity equation [Eq. (4)] gives the vorticity relation

$$\frac{\partial^2 v}{\partial t \partial x} + \beta v - \frac{f}{h} \left(\frac{\partial \tilde{\eta}}{\partial t} + h'u \right) = -\frac{r}{h^2} \left(\frac{\partial v}{\partial x} h - h'v \right), \quad (5)$$

where prime denotes d/dx . On the left hand side, the first term relates to relative vorticity, the second to the advection of planetary vorticity, the third to stretching of vorticity and the term on the right-hand side to vorticity induced by bottom friction—a source such as wind stress or a boundary condition could be included as an additional right-hand-side term. Alternatively, using Eqs. (2) and (3) to rewrite in terms of $\tilde{\eta}$, a more useful quantity in this context, we get

$$\frac{\partial^3 \tilde{\eta}}{\partial t \partial x^2} + \beta \frac{\partial \tilde{\eta}}{\partial x} + \left(\frac{fh'}{h} \frac{\partial \tilde{\eta}}{\partial y} + \frac{h'}{h} \frac{\partial^2 \tilde{\eta}}{\partial t \partial x} - \frac{1}{L_d^2} \frac{\partial \tilde{\eta}}{\partial t} \right) = -\frac{r}{h} \frac{\partial^2 \tilde{\eta}}{\partial x^2}, \quad (6)$$

where $L_d = (gh)^{1/2}/f$ is the external Rossby radius of deformation.

For the flat-bottom 1.5-layer vertical-sidewall scenario with $f = \beta y$, the terms involving h' disappear and L_d can be considered to be the internal Rossby radius L_d^{int} . As discussed by Clarke and Shi (1991), below a critical frequency, that is, for the low-frequency variability

considered here, the planetary vorticity term can come into balance with the stretching and relative vorticity terms, allowing Rossby waves at the boundary. Using this model Marshall and Johnson (2013) found a buoyancy anomaly to propagate along the boundary toward the equator as a short Rossby wave at the classical Kelvin wave speed $c = (gh)^{1/2}$, multiplied by $L_d^{\text{int}}/\delta_s$, where $\delta_s = r/\beta$.

Alternatively, for the sloping bottom with constant f scenario, we retain the stretching terms involving h' but lose the β term. The retained stretching terms are the topographic equivalent of β ; that is, the sloping bottom topography establishes a potential vorticity gradient. The balance between relative vorticity and stretching due to the bottom topography gives rise to shelf waves (topographic Rossby waves) (Salmon 1998, p. 73).

Wave solutions

In this study we are interested in the effect of retaining the stretching due to bottom topography terms, the advection of planetary vorticity β term and the friction term for annual-to-decadal variability. To this end, we simplify the model by making the rigid-lid approximation. For this, as in Gill and Schumann (1974), we assume that the Rossby radius of deformation L_d is larger than the cross-shore scale of the boundary response L , that is, $L_d \gg L$ and that the frequency of variability ω is restricted by $\omega \ll \beta L_d^2/L$. This allows the first term in the continuity equation [Eq. (4)], and therefore the third stretching term of the vorticity equation [Eq. (6)], to be neglected. This term is also small compared to the first stretching term and the term on the right-hand side of Eq. (6). With this approximation we have effectively filtered out the barotropic Kelvin wave response.

For the boundary conditions, we assume some specified anomaly along the poleward and interior boundaries; that is, $\tilde{\eta} = \tilde{\eta}_p$ at $y = y_p$ and $\tilde{\eta} = \tilde{\eta}_{\text{in}}$ at $x = x_{\text{in}}$, where throughout we use subscripts and superscripts “ p ” and “ in ” to refer to poleward and interior, respectively. The interior boundary condition is applied far enough away from the coast such that the boundary response has decayed west of it; that is, $x_{\text{in}} > L$. We consider $\tilde{\eta}_{\text{in}}$ as forcing due to the dynamics in the interior ocean, where basin-scale Rossby waves dominate the adjustment and hence $\tilde{\eta}_{\text{in}}$ can be thought of as describing a long Rossby wave incident on the western boundary. Similarly $\tilde{\eta}_p$ defines the forcing from a poleward (higher latitude) region; see Fig. 3. As the coast is approached, $x \rightarrow 0$, and we have $h \rightarrow 0$, which leads to $rv \rightarrow 0$ from Eq. (3) and then $\partial \tilde{\eta}/\partial x \rightarrow 0$ from Eq. (2). The boundary value problem can then be defined as

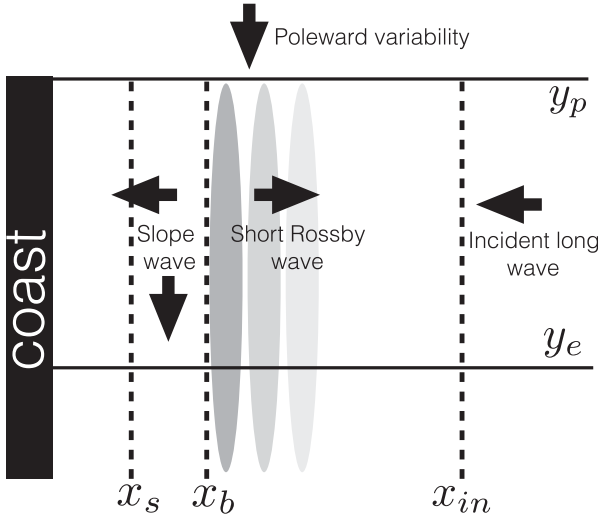


FIG. 3. Schematic illustrating the idealized domain, with variability imposed at the poleward boundary y_p and at the interior boundary x_{in} between the latitudes y_p and y_e , where y_e is equatorward of y_p . The shelf break and slope bottom are denoted by x_s and x_b . The arrows indicate the energy fluxes involved.

$$\frac{\partial^3 \tilde{\eta}}{\partial t \partial x^2} + \beta \frac{\partial \tilde{\eta}}{\partial x} + \frac{h'}{h} \left(f \frac{\partial \tilde{\eta}}{\partial y} + \frac{\partial^2 \tilde{\eta}}{\partial t \partial x} \right) = -\frac{r}{h} \frac{\partial^2 \tilde{\eta}}{\partial x^2}, \quad (7)$$

$$\frac{\partial \tilde{\eta}}{\partial x} \rightarrow 0 \quad \text{at} \quad x \rightarrow 0, \quad (8)$$

$$\tilde{\eta} = \tilde{\eta}_{in}(y, t) \quad \text{at} \quad x = x_{in}, \quad \text{and} \quad (9)$$

$$\tilde{\eta} = \tilde{\eta}_p(x, t) \quad \text{at} \quad y = y_p, \quad (10)$$

and we seek solutions in the form $\tilde{\eta}(x, y, t) = \eta(x, y)e^{-i\omega t}$.

The solution method, which to the authors' knowledge is somewhat novel and potentially useful, is derived in [appendix A](#). For clarity we simply state the solution below.

The solution of Eqs. (7)–(10) is

$$\eta(x, y) = \eta_{in}(y) - \sum_{j=1}^{\infty} \gamma_j C_j(x) A_j^{in}(y) + \sum_{j=1}^{\infty} \alpha_j C_j(x) A_j^p(y) \quad \text{with} \quad (11)$$

$$A_j^p(y) = \left(\frac{y}{y_p} \right)^{\lambda_j} \quad \text{and} \quad (12)$$

$$A_j^{in}(y) = \int_y^{y_p} \frac{d\eta_{in}}{ds} \left(\frac{y}{s} \right)^{\lambda_j} ds, \quad (13)$$

where γ_j , α_j , and λ_j are complex constants, $C_j(x)$, $A_j^p(y)$, and $A_j^{in}(y)$ are complex, and s is a dummy integration variable. Given that $\tilde{\eta}(x, y, t) = \eta(x, y)e^{-i\omega t}$, the real part of Eq. (11) describes the adjustment at the boundary as the summation of three sets of waves, with subscript j denoting the wave mode number. Note that throughout, we use $\Re(\cdot)$ and $\Im(\cdot)$ to denote real and imaginary parts of complex numbers; that is, $z = \Re(z) + i\Im(z)$.

The first term in Eq. (11) is the incident long wave from the interior, the second term is a set of waves excited by the incident wave from the interior, and the third term is a set of waves excited by the poleward forcing. For the second and third terms, $C_j(x)$ defines the j th wave mode's cross-shore structure. Note that the first two terms disappear when $\eta_{in} = 0$ and the third term disappears when $\eta_p = 0$ (α_j will be zero).

For our purposes it is enough to consider γ_j and α_j as constants that simply scale and phase shift each wave, we do not consider them further. The constants λ_j are the eigenvalues of an eigenvalue problem and are dependent on the topography, friction parameter, and frequency of variability.

Each wave mode has a specific alongshore decay rate and phase and we have ordered the modes according to the decay rate, that is, the magnitude of $\Re(\lambda_j)$, where $0 < \Re(\lambda_1) < \Re(\lambda_2) < \Re(\lambda_3) < \dots < \Re(\lambda_n)$, for $n \rightarrow \infty$. For waves excited from poleward, this orders the modes according to their alongshore decay rate, such that the first wave mode $j = 1$ propagates farthest.

Apart from where specified otherwise, we use the parameter configuration defined in [Table 1](#) for calculations. The configuration has been chosen to be somewhat representative of reality and we note the friction parameter is small to investigate weak damping, which helps elucidate the wave structures, though we also explore stronger damping.

Note that our boundary wave assumption fails as we approach the equator, where waves cease to be trapped to the boundary. Context determines how close to the equator this failure occurs. For example, in a purely barotropic ocean we would expect an equatorial barotropic Rossby radius to be the relevant scale (around 2000 km in water that is 4 km deep). If, instead, we are

TABLE 1. Parameter configuration used throughout unless explicitly stated otherwise. The final three columns are the short Rossby wavelength and the respective Rossby radii of deformation for shelf and open-ocean depths, with $f = 10^{-4} \text{ s}^{-1}$.

ω (s^{-1})	r (m s^{-1})	x_s (km)	x_b (km)	H_s (m)	H_b (m)	β ($\text{m}^{-1} \text{ s}^{-1}$)	$2\pi\omega/\beta$ (km)	$(gH_s)^{1/2}/f$ (km)	$(gH_b)^{1/2}/f$ (km)
10^{-7} (24 months)	0.000 02	100	130	100	4100	1.667×10^{-11}	37.7	310	2000

considering the boundary processes to represent the upper layer of a two-layer system, the situation is less clear. Accordingly, we present results all the way to the equator but caution that interpretation is uncertain close to the equator.

3. Cross-shore wave structure

From Eq. (11), we note that the cross-shore structures of the wave modes $C_j(x)$ are the same irrespective of whether they are excited by poleward or interior forcing. In contrast to inviscid f -plane shelf waves, which only propagate along the shelf, there is now a cross-shore contribution to the phase, denoted by $\varphi_j^x(x) = \arg[C_j(x)]$. The cross-shore component of the wave amplitude is $|C_j(x)|$, where we use $||$ to denote the magnitude of a complex number.

Figure 4 shows the real and imaginary parts of the first nine wave modes, $\Re(C_j)$ and $\Im(C_j)$, $j = 1, 2, \dots, 9$, each normalized by maximum amplitude. The waves can be classified into two classes of wave based on their dominant characteristics. First, wave modes 1, 2, 6, and 9 decay on the shelf with little or zero amplitude off-shelf. These waves are akin to topographically trapped f -plane shelf waves (Robinson 1964; Huthnance 1975), where the number of offshore nodes (zero amplitudes) increases with mode number. Here the shelf waves are subject to modification by the inclusion of bottom friction and the β effect. We label this group of waves (viscous) β -plane shelf waves. The second group of waves, modes 3, 4, 5, 7, and 8, are by contrast characterized by a significant offshore component where the wavenumber is, to a first approximation, that of the inviscid short Rossby wave,

$$\frac{d}{dx}(\varphi_j^x) \approx -\frac{\beta}{\omega}, \quad \text{for } x > x_b. \quad (14)$$

This is approximate because frictional damping will also have a contribution. These waves have a structure on the slope, for example, for higher mode slope waves $d\varphi_j^x/dx \sim 10^{-4} \text{ m}^{-1}$ on the slope, and we label this group as “leaky slope waves.” Figure 4 also shows the imaginary parts of the waves, giving a sense of the zonal phase lag, for example the westward phase propagation of the short Rossby component of the waves, although we do not discuss this further.

For the higher-mode-number waves that are not shown, that is, $j > 9$, we find that each wave fits, with increasing fidelity, into one or the other group, giving essentially two sets of wave types: β -plane shelf waves (1, 2, 6, and 9) and leaky slope waves (3, 4, 5, 7, and 8). With this classification made, we note two points. First, wave modes can be said to exhibit characteristics

from both types of wave (particularly lower modes), however for the purposes of exploring boundary adjustment processes, it is helpful to group them by their dominant characteristics. Second, we note that, while the wave modes shown in Fig. 4 are naturally specific to the parameter regime we have chosen, the two wave types, as described above, have been found to be general within the scope of the parameter space used in this study. It is worth noting, however, that as the friction parameter is increased the short Rossby component becomes damped and a Stommel-like frictional boundary layer expands offshore instead. Beyond the additional scenario of very-long-time-period variability, $\omega \ll r/H$, an exhaustive parameter study is beyond the scope of this paper. From here onward we will use mode 5 to represent the set of leaky slope waves and mode 6 to represent the set of β -plane shelf waves; we will also include mode 1 in the discussion because it proves to play a somewhat special role in the overall boundary response.

In the following sections we will look at the along-shore wave evolution and energetics for the cases of poleward and interior variability.

4. Forcing from poleward

a. Alongshore evolution

When the waves are generated by variability from higher latitudes, Eq. (11) reduces to

$$\tilde{\eta}(x, y, t) = \sum_{j=1}^{\infty} \alpha_j C_j(x) A_j^p(y) e^{-i\omega t} \quad \text{and} \quad (15)$$

$$A_j^p(y) = \left(\frac{y}{y_p}\right)^{\Re(\lambda_j)} \exp[i\Im(\lambda_j) \ln(y/y_p)], \quad (16)$$

where A_j^p gives the alongshore wave evolution and we have separated λ_j into real and imaginary parts to explicitly show the amplitude and phase components.

Preemptively assuming, for a moment, that $\Re(\lambda_j) > 0$ for all j , the relation in Eq. (16) describes the wave amplitudes as decaying alongshore in the direction of the equator (note that $(y/y_p) \leq 1$). The physical limitations of the model close to the equator are important avenues for future research—that is, nonlinear effects and stratification should become important; however, for the solutions presented here we can make use of the vorticity equation [Eq. (7)] to justify the above assumption.

Separating variables in Eq. (7) by substituting $\tilde{\eta}(x, y, t) = C(x)A^p(y)e^{-i\omega t}$ yields the generalized eigenvalue problem

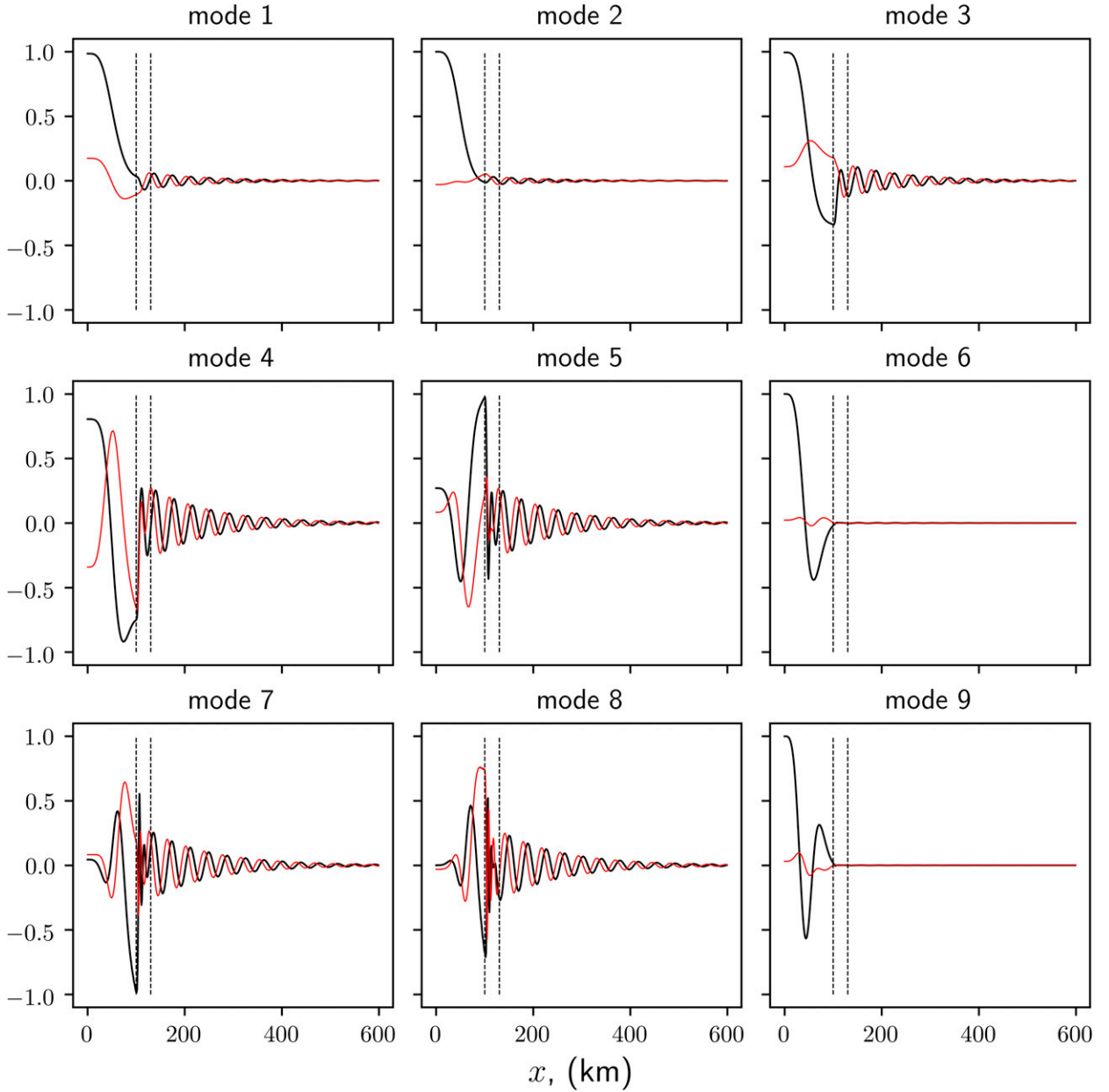


FIG. 4. Cross-shore structure of the first nine wave modes, each normalized by its maximum amplitude $|C_j(x)|_{\max}$. Black corresponds to the real part of the x dependent part of the solution, $\Re[C_j(x)]$, and red corresponds to the imaginary part $\Im[C_j(x)]$. The dashed lines denote the shelf break at $x = x_s = 100$ km and slope bottom at $x = x_b = 130$ km.

$$(r - ih\omega)C'' + (h\beta - ih'\omega)C' = -\lambda h' C \quad (17)$$

subject to $C' = 0$ at $x = 0$ and $C = 0$ at $x = x_{in}$. For solutions of the form $C_j = |C_j(x)| \exp[i\varphi_j(x)]$, substitution into Eq. (17) and taking the real parts gives

$$-\Re(\lambda_j)h'|C_j| = 2\omega h|C_j|\varphi_j' + \omega h|C_j|\varphi_j'' + \omega h'|C_j|\varphi_j' + \beta h|C_j|' + r|C_j|'' - r|C_j|(\varphi_j')^2. \quad (18)$$

Using integration by parts and the boundary conditions, the right-hand side (RHS) of $\int_0^{x_{in}} [\text{Eq. (18)}]|C_j| dx$ is ≤ 0 . Given that the left-hand side (LHS) of $\int_0^{x_{in}} [\text{Eq. (18)}]|C_j| dx$ must also be ≤ 0 and that $\int_0^{x_{in}} h'|C_j|^2 dx \geq 0$, it is true that $\Re(\lambda_j) \geq 0$. Hence all wave modes decay in amplitude in the direction of the equator. Later we will argue to further restrict this lower bound to $\Re(\lambda_j) \geq 1$ such that $1 \leq \Re(\lambda_1) < \Re(\lambda_2) < \Re(\lambda_3) < \dots < \Re(\lambda_n)$, for $n \rightarrow \infty$. This implies that all modes have decayed to zero at the

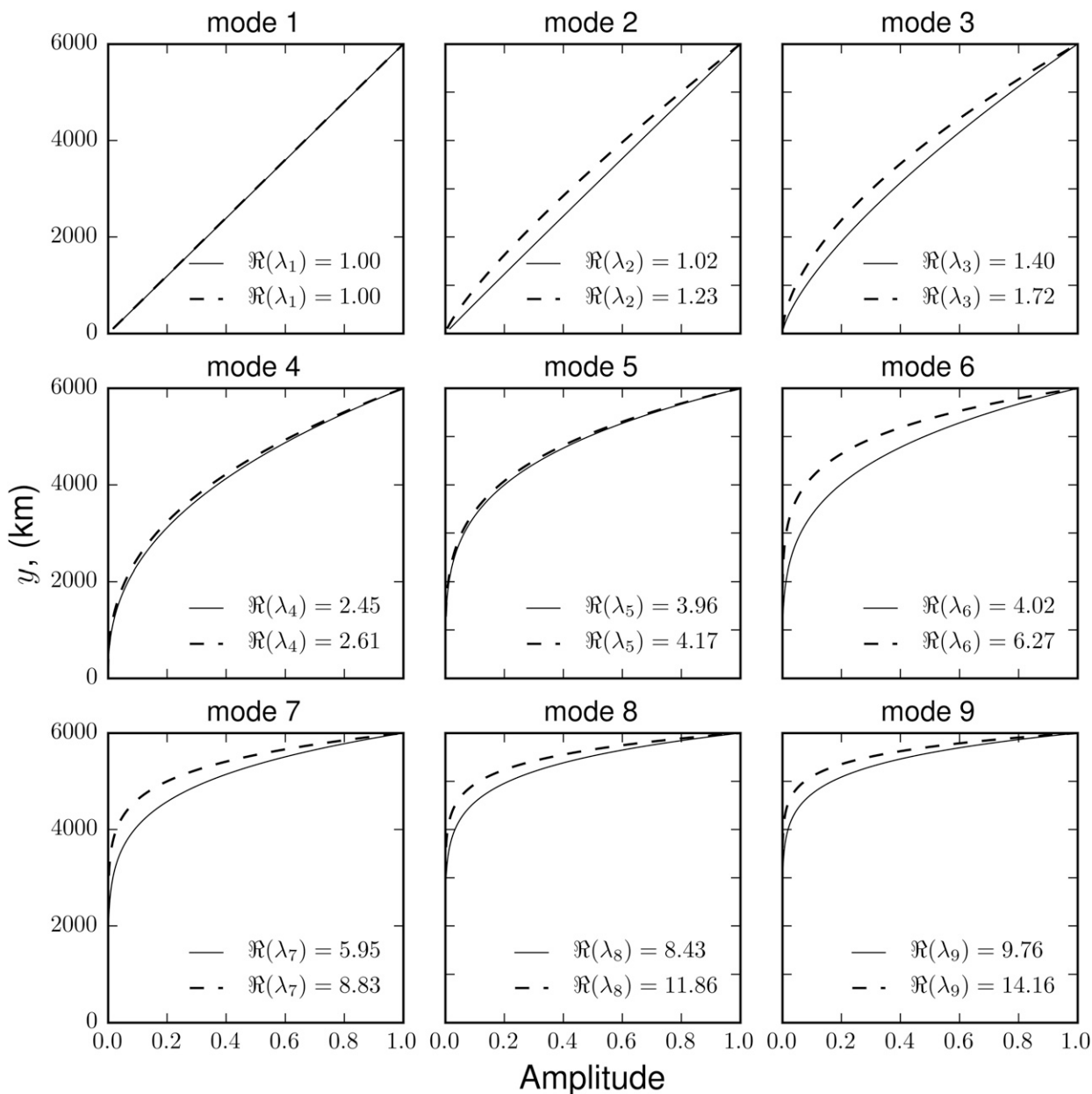


FIG. 5. Alongshore amplitude $(y/y_p)^{\Re(\lambda_j)}$ of the first nine wave modes, $j = 1, 2, \dots, 9$, where solid lines denote a shelf width of 100 km and dashed lines denote a shelf width of 20 km; $y = y_p$ is 6000 km poleward of the equator at $y = 0$.

equator and that, for example, mode 2 will decay farther from the equator than mode 1.

The solid lines in Fig. 5 show the alongshore amplitude $(y/y_p)^{\Re(\lambda_j)}$ for the first nine wave modes, together with the value of $\Re(\lambda_j)$. The first-mode decay is approximately linear, $\Re(\lambda_j) \approx 1$, and the decay rate increases as mode number increases. Figure 6a shows the solution $\tilde{\eta}(x, y, t)$ at time $t = 0$ between two latitudes y_p and y_e , where subscript e denotes equatorward, for $j = 1, 2, \dots, 1000$ with the poleward-forcing

constant on the shelf and slope, $\eta_p = -1$, such that $v = 0$ at y_p on the shelf and slope. Note how the amplitude decays on the slope in the direction of the equator as fewer modes contribute to the boundary response and how this effectively allows the interior amplitude, which in this case is zero, to penetrate onto the slope at lower latitudes (between the dashed lines: it is dark blue at the poleward boundary and pale blue at the equatorward boundary).

We noted previously that λ_j are dependent on the parameters $h(x)$, r , and ω . The dashed lines in Fig. 5

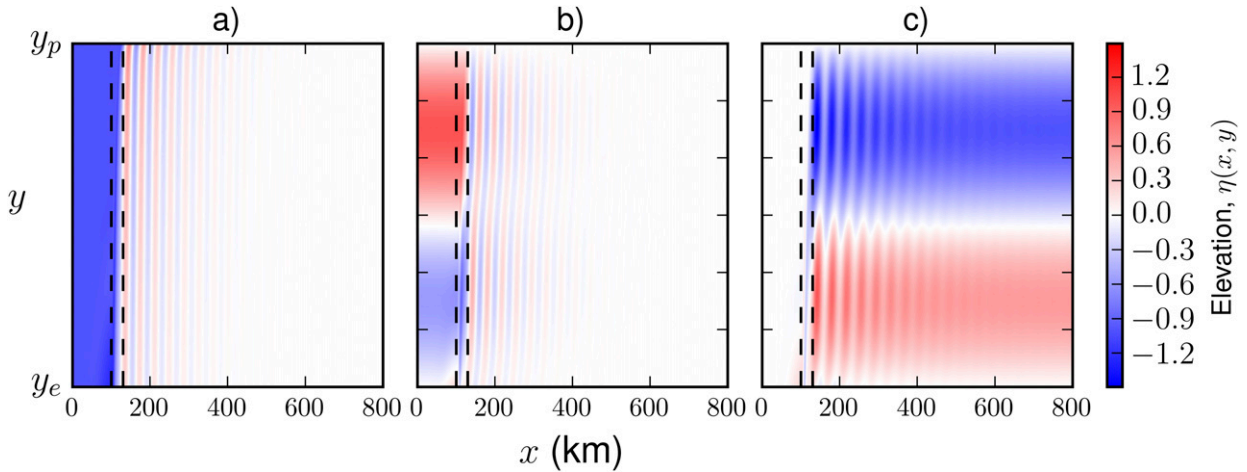


FIG. 6. (a) Sum of all wave modes $\sum_j \alpha_j C_j(x) A_j^p(y)$, for a poleward forcing at y_p that is constant on the shelf and slope $\eta_p = -1$ and tends smoothly to zero east of the slope. (b) Sum of all wave modes $-\sum_j \gamma_j C_j(x) A_j^{\text{in}}(y)$ when forced by an interior representing a double gyre (see dashed line η_{in} in Fig. 10b, below). (c) Incident long wave from the interior plus the sum of waves shown in (b), i.e., $\eta_{\text{in}} - \sum_j \gamma_j C_j(x) A_j^{\text{in}}(y)$. In (a)–(c), time $t = 0$, vertical dashed lines denote shelf break and slope bottom, and y_p and y_e are 6000 and 3000 km poleward of the equator, respectively.

show the alongshore amplitudes when the shelf width has been decreased to 20 km (solid lines are for a shelf width of 100 km). The alongshore amplitude decay rate (in space and not time) increases for all modes except mode 1. A relatively small increase in $\Re(\lambda_j)$ can significantly shorten the length scale over which the wave decays. Figure 7a compares $\Re(\lambda_j)$ for the first 40 wave modes for shelf widths of 100 and 20 km. As the shelf width decreases, higher wave modes decay at increasingly high latitudes and in effect become negligible for the overall boundary response. The narrower shelf width acts to filter out higher wave modes from the

boundary response. A narrower shelf also tends to decrease wave propagation speed [increasing the magnitudes of $\Im(\lambda_j)$]. Hence slower wave propagation, and the decay of the wave amplitude over a shorter alongshore distance, result from a narrower shelf. This is consistent with the results of Huthnance (1987), where an f plane is used.

This result implies that a high-latitude pressure anomaly propagates farther toward the equator when the shelf is wider. It also suggests, as we will discuss in the following section, that information from the interior ocean will give a relatively larger contribution to the coast when the shelf

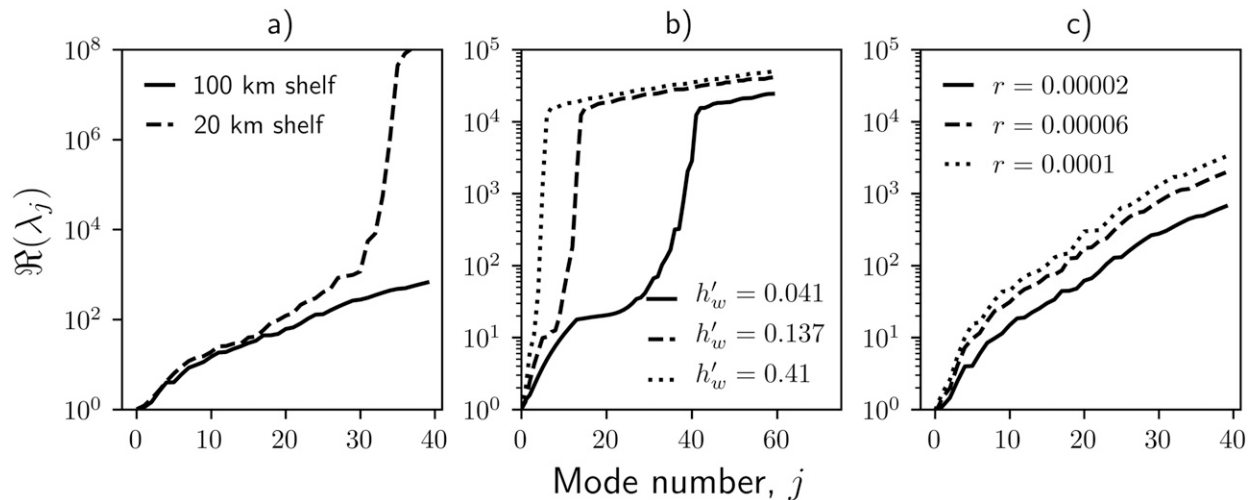


FIG. 7. Semilog plots: (a) the first 40 $\Re(\lambda_j)$ for two shelf widths; (b) the first 60 $\Re(\lambda_j)$ for a sloping sidewall bottom topography (see Fig. 2b) for three different sidewall gradients h'_w , i.e., $H_b = 4100$ m and $x_b = 100$ (solid), 30 (dashed), or 10 (dotted) km; and (c) the first 40 $\Re(\lambda_j)$ for three different values of the friction coefficient r , with the standard shelf and slope configuration.

is narrower. In Fig. 6a this would be seen as the shelf and slope amplitudes decaying toward zero farther away from y_e , that is, greater penetration from the interior. Coastal bathymetry is often represented coarsely in numerical models and with a vertical wall in conceptual models. These results suggest that the representation of bathymetry could be a source of difference between OCM simulations of western boundaries.

The consequences of using a vertical sidewall can be shown more explicitly by considering the decay rate of waves for the case of a sloping sidewall at the boundary (schematic Fig. 2b) when the gradient of the sloping sidewall h'_w is increased. Figure 7b compares $\Re(\lambda_j)$ for the first 60 wave modes when the sloping sidewall has three different gradients: $h'_w = 0.041, 0.137, \text{ and } 0.41$, where a larger gradient equates to a steeper sidewall. As the sloping sidewall steepens, the magnitudes of $\Re(\lambda_j)$ increase and fewer wave modes contribute to the boundary response. Indeed in the steepest case (sidewall depth 4100 m and width 10 km), only the first five modes are effectively contributing to the boundary response.

An important exception to this dependency on bottom topography is the mode-1 wave. For all sidewall gradients, $\Re(\lambda_1) \approx 1$. Decreasing the shelf width (steepening) is compensated for by changes in the cross-shore wave structure as frictional effects increase. In the steep slope limit, where the sloping sidewall tends to vertical, all modes except mode 1 are effectively “killed off” and a single mode remains. In the absence of topographic effects, this mode decays alongshore proportionally to f such that, as we will see, the zonal energy flux is constant with latitude. This is consistent with Marshall and Johnson (2013) who found only a single wave decaying linearly alongshore in their vertical-sidewall model. The reason mode 1 is so similar to the first baroclinic wave of Marshall and Johnson (2013) is that the mode-1 wave is effectively a rigid-lid version of the free-surface wave, maintaining no horizontal divergence across the domain. For low-frequency forcing, the first baroclinic wave is, relatively, very fast (i.e., relative to the time scale for forcing, the boundary adjustment is quick and soon comes into equilibrium), here with the rigid lid, mode 1 does this effectively instantaneously. Note that this rigid-lid response can be split across multiple modes. The important point is that by filtering out higher wave modes from the boundary response, the vertical sidewall is a limit where the propagation of variability from higher to lower latitudes is minimized.

The choice of friction parameter can affect the boundary response in a similar fashion. Figure 7c compares $\Re(\lambda_j)$ for the first 40 modes for three values of the friction parameter

r , using the standard shelf configuration. Increasing the friction parameter is found to increase the magnitudes of $\Re(\lambda_j)$ and therefore effectively decreases the number of modes contributing to the boundary response, as described above. Once again mode 1 remains the exception with $\Re(\lambda_1) \approx 1$. Increasing the friction parameter is compensated for by an increase in the boundary layer width. In the large friction limit, the boundary layer width becomes large compared to the width of the topography and higher modes are killed off, leaving a single wave that decays proportionally to f (topographic effects have become small). As has been discussed by Deremble et al. (2017), the dynamical justification for the subgrid-scale parameterization of viscosity in OCMs is somewhat opaque and can be a source of inconsistency between simulations, for example, Gulf stream separation point (Bryan et al. 2007). The dependency of the waves on the friction parameter r is a plausible mechanism for some of this inconsistency. This issue is somewhat lost in vertical-sidewall models, which already filter out the higher wave modes. Indeed Marshall and Johnson (2013) found the wave amplitude to be independent of the friction parameter in their vertical-sidewall model. These parameter sensitivities should also broadly apply to the f plane.

From Eq. (16) the alongshore phase component of the waves is given by $\varphi_j^y(y) = \Im(\lambda_j) \ln(y/y_p)$, which grows in magnitude in the direction of the equator. For wavenumber $d\varphi_j^y/dy$, slope waves are typically shorter than shelf waves, with the mode-5 slope wave of order 10^{-6} m^{-1} and the mode-6 shelf wave of order 10^{-7} m^{-1} , for example. The mode-5 wave speed is therefore $\sim 0.01 \text{ m s}^{-1}$, and the mode-6 wave speed is $\sim 0.1 \text{ m s}^{-1}$. In general, the higher the shelf or slope mode number is, the shorter the wave becomes. Given that the amplitude decay distance is of order 10^6 m alongshore and of order 10^5 m cross-shore, the geostrophic assumption in Eq. (2) appears to be valid with $(\omega/f)(\partial_y/\partial_x) \ll 1$. Modes 1 and 2 can be very long for weak damping ($\sim 10^{-9}$ to 10^{-10} m^{-1}). Increasing the friction parameter or steepening the topography typically results in slower wave propagation. The exception here is mode 1, which, as we have noted, does not decay over shorter length scales as damping or topographic steepness increase. Instead, the mode-1 wavenumber tends to becoming vanishingly small as damping increases and the solution tends to a Stommel-like boundary solution.

An interesting consequence of allowing f to change with latitude is that waves no longer strictly propagate equatorward. This can be shown from the eigenvalue problem introduced in Eq. (17). For solutions of the form $C_j = |C_j(x)| \exp[i\varphi_j(x)]$,

substitution into Eq. (17) and taking the imaginary parts gives

$$-\Im(\lambda_j)h'|C_j| = 2r|C_j|\phi'_j + r|C_j|\phi''_j - h'\omega|C_j|' + h\omega|C_j|(\phi'_j)^2 - h\omega|C_j|'' + \beta h|C_j|\phi'_j. \quad (19)$$

Multiplying through by $|C_j|$ and integrating over x then gives

$$-\Im(\lambda_j)\int_0^{x_{in}} h'|C_j|^2 dx = \omega\int_0^{x_{in}} h(|C_j|')^2 dx + \omega\int_0^{x_{in}} h|C_j|^2(\phi'_j)^2 dx + \beta\int_0^{x_{in}} h|C_j|^2\phi'_j dx, \quad (20)$$

where we have used integration by parts and the boundary conditions to simplify. The first and second terms on the RHS of Eq. (20) are ≥ 0 , but the sign of the third term depends on ϕ'_j . Given that the integral on the LHS is ≥ 0 , the sign of $\Im(\lambda_j)$ will depend on ϕ'_j . Hence wave propagation is strictly poleward [$\Im(\lambda_j) \geq 0$] if 1) $\phi'_j \leq 0$ for all x (westward phase propagation) and 2) the third term on the RHS is larger in magnitude than the sum of the first and second terms on the RHS. We have found these conditions can be met for modes 1 and 2 when damping is weak, although this may be a spurious artifact of the rigid-lid approximation, as noted above.

An important consequence of the latitude dependence and parameter sensitivity of alongshore amplitude and phase, is that phase speed is a potentially poor measure of information propagation, amplifying a similar conclusion by Marshall and Johnson (2013).

b. Energetics

The velocity at which energy flows at the boundary can be considered as the velocity at which information flows. We are therefore interested in the energy flux of the boundary response. Multiplying the momentum and continuity equations [Eqs. (2), (3), and (4)] by ρu , ρv , and $\rho g\eta$, respectively, and adding together the three resulting equations gives the energy equation

$$h\frac{\partial}{\partial t}\left(\frac{\rho v^2}{2}\right) + \nabla \cdot \rho gh\tilde{\eta}\mathbf{u} = -\rho rv^2. \quad (21)$$

In the steady state, the divergence of the energy flux $\nabla \cdot \rho gh\tilde{\eta}\mathbf{u}$ balances dissipation $-\rho rv^2$ and we denote the time averaged energy flux as $\rho gh\tilde{\eta}\mathbf{u} = (\tilde{F}^x, \tilde{F}^y)$.

Using geostrophic balance for v and Eqs. (3) and (15) for u and $\tilde{\eta}$, respectively, the divergent time-averaged energy flux is

$$(F^x, F^y) = -\frac{\rho g^2}{4}\left\{\left[\frac{r}{f^2}\frac{\partial}{\partial x}(|\eta|^2) + \frac{2h\omega}{f^2}|\eta|^2\frac{\partial\phi}{\partial x}\right]\hat{\mathbf{i}} + |\eta|^2\hat{\mathbf{k}} \times \nabla\left(\frac{h}{f}\right)\right\}, \quad (22)$$

where a nondivergent part, $\hat{\mathbf{k}} \times \nabla(|\eta|^2 h/f)$, has been excluded (Longuet-Higgins 1964). Written in this way, the flux consists of a purely zonal component and a component along h/f contours that is directed toward the west and equator. The meridional component, which is always directed equatorward, is

$$F^y = -\frac{\rho g^2 h'}{4f}|\eta|^2. \quad (23)$$

Figure 8a shows the meridional flux at each longitude as a fraction of the total equatorward flux per meter of latitude for the boundary response presented in Fig. 6a, that is, for the sum of all wave modes. The energy flows as a jet along the slope toward the equator—the steep topographic gradient on the slope supports the strong alongshore velocity and hence kinetic energy.

The zonal component of the flux is

$$F^x = -\frac{\rho g^2}{4f^2}\left[r\frac{\partial}{\partial x}(|\eta|^2) + 2h\omega|\eta|^2\frac{\partial\phi}{\partial x} + h\beta|\eta|^2\right], \quad (24)$$

and Fig. 8b shows the fraction of total equatorward flux at y_p that is fluxed zonally across each longitude (m^{-1} of longitude). On the slope, the energy flows toward the shelf break, whereas offshore of the slope, the energy flow is toward the interior. The primary energy flow can therefore be described as an equatorward jet along the slope, which leaks out eastward into the interior. This is very different from the meridional energy flow expected of an f -plane, inviscid solution, in which the shelf waves propagate along-shelf without decaying.

In general, the energy flux cannot be separated into contributions from the individual wave modes because of the interactions between waves. However, with each mode satisfying the governing equations, it remains insightful to consider the fluxes of the individual waves, recalling that mode 6 represents β -plane shelf waves and mode 5 represents leaky slope waves. Figures 9a–c show the meridional fraction of total equatorward flux (m^{-1}) for wave modes 1, 5, and 6, respectively. Figures 9a and 9c show that the shelf waves transmit energy equatorward along the shelf, whereas Fig. 9b shows that slope waves transmit energy equatorward along the slope. Figures 9d–f show, for the same three modes, the fraction of total equatorward flux at y_p that is fluxed zonally across each longitude (m^{-1}) at two different latitudes, y_p and y_e , where e denotes a latitude equatorward of y_p .

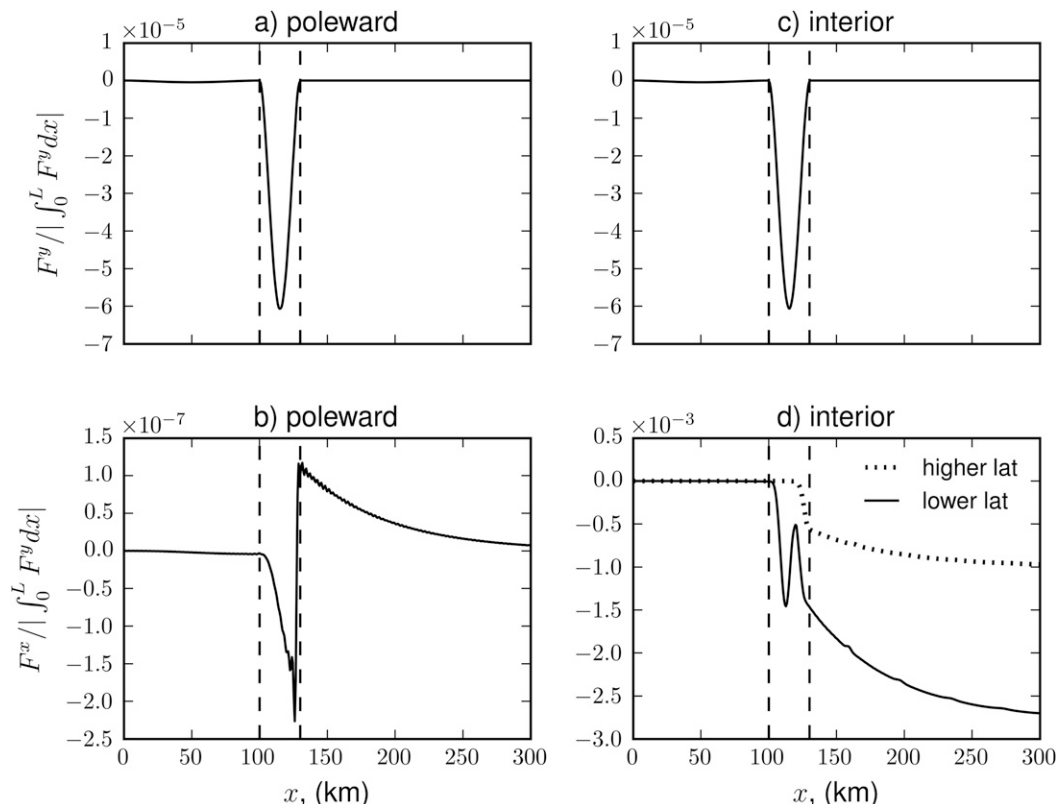


FIG. 8. Energy fluxes for the full solutions shown in Figs. 6a and 6c: (a) meridional flux as a fraction of total equatorward flux (m^{-1} of latitude) for the case of poleward variability, (b) zonal flux as a fraction of total equatorward flux (m^{-1} of longitude) at $y \rightarrow y_p$ for the case of poleward variability, (c) meridional flux as a fraction of total equatorward flux (m^{-1} of latitude) for the case of interior variability, and (d) zonal flux at two different latitudes as a fraction of total equatorward flux at $y \rightarrow y_p$ (m^{-1} of longitude) for the case of interior variability. In (d), the zonal fluxes are taken at a high latitude (dotted curve) and lower latitude (solid curve), where $|\eta_{in}| = 0.5$.

Figures 9d and 9f show that the shelf waves transmit energy across the shelf, whereas Fig. 9e shows that the leaky slope waves transmit energy from the slope onto the shelf and into the interior. The dashed lines show that the zonal flux decreases at lower latitudes for modes 5 and 6. With the amplitude of the shelf waves decaying on the shelf, it is the leaky slope waves that are responsible for the main energy pathway, shown as a schematic in Fig. 3.

Clearly the leaky slope waves are not topographically trapped but instead radiate Rossby waves offshore, which then decay as a result of dissipation. In the limit of small dissipation, the open-ocean energy flux becomes the product of energy density and the group speed of short Rossby waves.

The fluxes of the individual waves decrease at lower latitudes according to

$$(F^x, F^y) \propto [(y/y_p)^{2\Re(\lambda_j)-2}, (y/y_p)^{2\Re(\lambda_j)-1}]. \quad (25)$$

For mode 1, assuming $\Re(\lambda_1) \approx 1$, the zonal flux is approximately constant through all latitudes and the meridional

flux decreases approximately linearly to zero at the equator. As mode number increases, the zonal and meridional fluxes both decay at lower latitudes at a higher, nonlinear, rate. These rates increase when the friction parameter is increased or when the width of the shelf is decreased.

Energy is lost to dissipation at an alongshore rate

$$\int_0^L r v^2 dx = \left(\int_{\text{shelf}} + \int_{\text{slope}} + \int_{\text{off-slope}} \right) \nabla \cdot gh \tilde{\eta} \mathbf{u} dx, \quad (26)$$

where the zonal integral has been split into the shelf, slope, and east-of-slope components. For shelf waves, the integrals across the slope and offshore are small. The slope waves, by contrast, dissipate energy on the slope as well as off-slope. Hence along western boundaries the β effect and friction enable an additional energy pathway and an increased dissipation rate, with the effect that high-latitude variability has a reduced footprint at lower latitudes. Relative to a vertical-sidewall model, more energy is fluxed equatorward and there is less dissipation at higher latitudes; however,

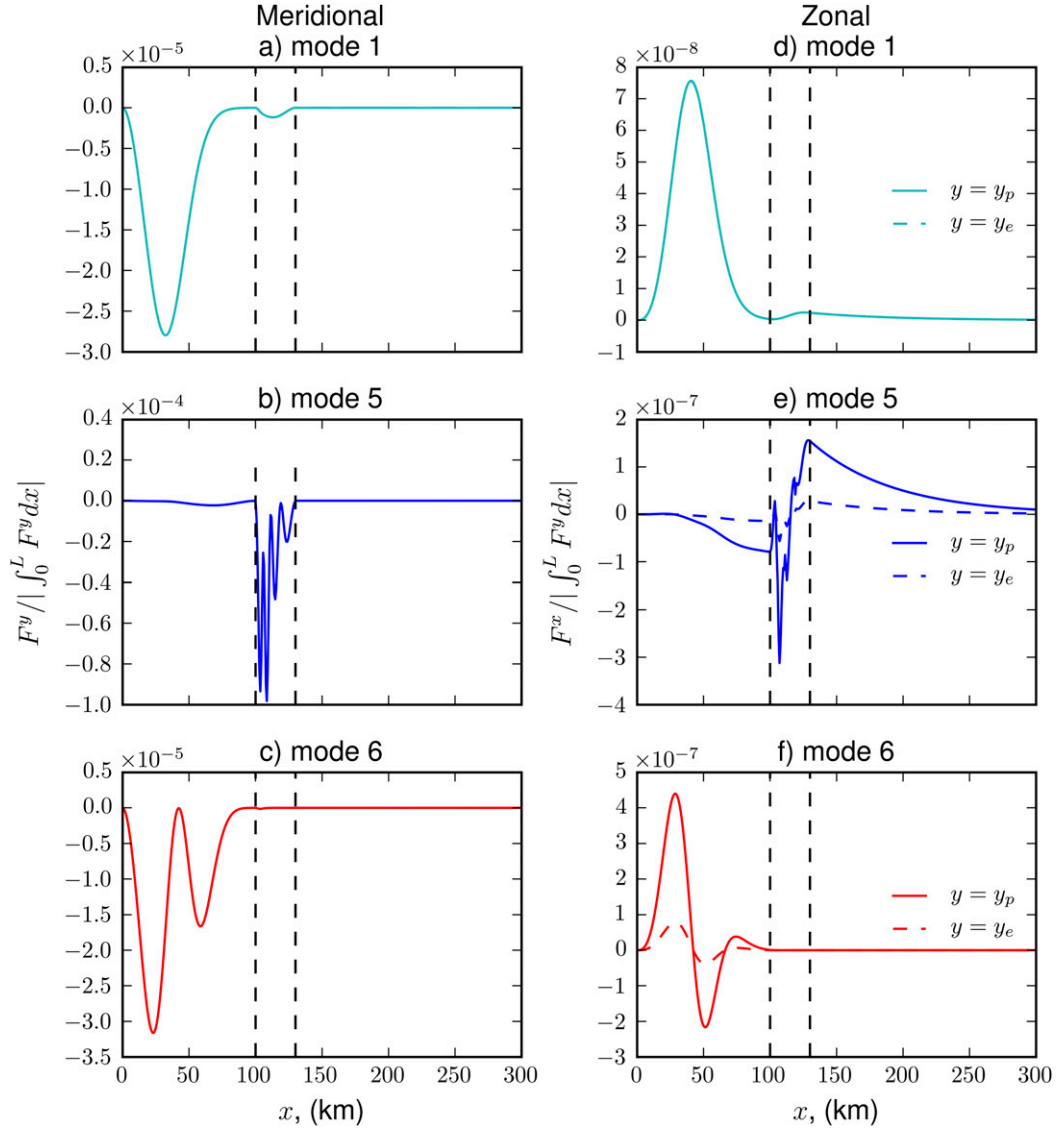


FIG. 9. For the poleward-forcing case, the meridional flux as a fraction of total equatorward flux (m^{-1} of latitude) for wave modes (a) 1, (b) 5, and (c) 6, respectively. (d)–(f) The corresponding zonal flux at two different latitudes as a fraction of total equatorward flux at $y \rightarrow y_p$ (m^{-1} of longitude). For (d)–(f) the zonal fluxes are taken at a high latitude (solid curves) and midlatitude (dashed curves). Vertical black dashed lines denote the shelf break and slope bottom.

as the shelf width decreases or friction parameter increases, more energy is dissipated at higher latitudes.

To readdress the issue of the lower bound of $\Re(\lambda_j)$, we note that the alongshore dissipation rate of an individual mode is $\propto (y/y_p)^{2\Re(\lambda_j)-2}$. In this case, allowing $\Re(\lambda_j) < 1$ implies that the rate of energy lost to dissipation increases as latitude decreases, tending to infinity at the equator. This would imply that effectively all energy is lost precisely at the equator, which appears to be unreasonable. Although not a formal proof, taken together with numerous calculations, we assume it is reasonable to take $\Re(\lambda_j) \geq 1$. As previously noted, our assumption

of wave trapping breaks down as f becomes small, and we expect energy to leak into the equatorial waveguide and propagate eastward.

5. Forcing from the interior ocean

a. Alongshore evolution

When the boundary waves are excited by variability in the interior ocean, solution Eq. (11) reduces to

$$\tilde{\eta}(x, y, t) = \left[\eta_{\text{in}}(y) - \sum_{j=1}^{\infty} \gamma_j C_j(x) A_j^{\text{in}}(y) \right] e^{-i\omega t} \quad \text{and} \quad (27)$$

$$A_j^{\text{in}}(y) = \int_y^{y_p} \frac{d\eta_{\text{in}}}{ds} \left(\frac{y}{s}\right)^{\Re(\lambda_j)} e^{[i\Im(\lambda_j)\ln(y/s)]} ds, \quad (28)$$

where s is a dummy integration variable. Here $\tilde{\eta}$ is the net response at the western boundary where the excited boundary waves are added to the incident long wave η_{in} . The coast will be insulated from variability in the interior when the excited waves destructively interfere with the incident long wave, that is, when the sum of the excited waves cancels out the long wave on the shelf. Figure 6b shows the sum of excited waves when forced by a double-gyre interior (see Fig. 10b), and Fig. 6c shows the net response. The shelf is clearly insulated, particularly at higher latitudes, but the alongshore wave amplitudes are important in determining the extent to which the coastline is insulated.

Consider first the case in which the interior amplitude $\eta_{\text{in}}(y)$ increases linearly from latitude y_e to latitude y_p such that $\eta_{\text{in}}(y_e) < \eta_{\text{in}}(y_p) = 0$ and $d\eta_{\text{in}}/ds$ is constant and can be taken outside the integral in Eq. (28). At each latitude y between y_e and y_p , the excited wave amplitudes result from a summation (integral) of the effects poleward of y . For mode 1 this gives an alongshore amplitude very roughly proportional to η_{in} . For higher modes, where $\Re(\lambda_j)$ is larger, the amplitude is reduced and concentrated farther poleward. Figure 10 shows this clearly with the alongshore amplitudes for modes 1, 5, 6, and 12 for two interior scenarios: linear (Fig. 10a) and double gyre (Fig. 10b). In this manner, drawing on our previous analysis, we can see that increasing $\Re(\lambda_j)$, via a decreased shelf width or increased friction parameter, will lead to greater penetration of interior variability at the coast (and at higher latitudes) because the amplitude of the excited waves is reduced and concentrated farther poleward and thus will interfere less with the incident long wave.

Interestingly, unlike the amplitude of waves generated by poleward variability, the alongshore amplitude of waves excited by the interior depend on both $\Re(\lambda_j)$ and $\Im(\lambda_j)$. The important point is that the complex exponential cannot be taken outside the integral in Eq. (28) so that at each latitude s , poleward of y , the alongshore phase of the wave contributes to the equatorward amplitude. The smaller phase speed [larger $\Im(\lambda_j)$] of the slope waves relative to the shelf waves results in their decaying relatively farther poleward; for example, see modes 5 and 6 in Fig. 10.

b. Energetics with interior forcing

The energy flux of the net boundary response will now include interactions between the excited waves and the

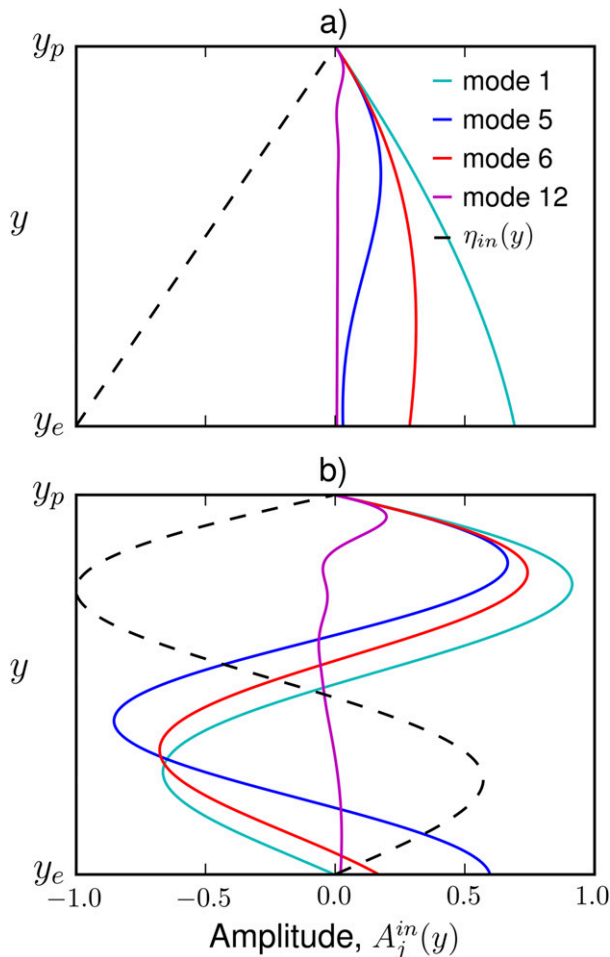


FIG. 10. Alongshore amplitude of waves excited by interior variability for modes 1, 5, 6, and 12, i.e., $A_j^{\text{in}}(y)$ for $j = 1, 5, 6,$ and 12 for two different interior amplitude profiles: (a) linear and (b) double gyre.

incident interior long wave. The long wave, by assumption, has no meridional velocity and therefore does not affect the longitudinal distribution of meridional flux as a fraction of the total equatorward flux (see Fig. 8c). The situation is different for the zonal fraction of the energy flux, where the incident wave contributes a westward flux. Figure 8d shows the zonal fraction of the equatorward flux at y_p for two different latitudes: a high latitude where $\eta_{\text{in}} = -0.5$ (dotted line) and a lower latitude where $\eta_{\text{in}} = 0.5$ (solid line). Clearly the energy due to the incident wave penetrates onshore to a greater extent at lower latitudes, although the excited wave contribution is clearly visible.

The zonal and meridional fluxes of the individual excited waves remain as given by Eqs. (24) and (23), and the energy pathways of the waves remain as shown in Fig. 9. The latitude dependency of the fluxes now becomes

$$(F^x, F^y) \propto (|A_j^{\text{in}}|^2/f^2, |A_j^{\text{in}}|^2/f), \quad (29)$$

implying that the alongshore decay rate of the energy fluxes increases with mode number. Increasing the friction parameter or decreasing the width of the bottom topography will increase the alongshore decay rate of the fluxes of all modes, except mode 1.

The dissipation of shelf and slope waves excited by forcing in the interior ocean is a mechanism by which western boundaries can act as a sink of energy in the ocean energy budget, and is consistent with the Rossby “graveyard” idea (Zhai et al. 2010). Energy incident from the interior results in an equatorward jet of energy on the slope and leakage of energy back toward the interior as radiating short Rossby waves and also onto the shelf (see schematic Fig. 3). Decreasing the width of the shelf or increasing the friction parameter reduces the equatorward flux and increases dissipation at high latitudes as the higher wave modes decay at higher latitudes. While section 4 showed energy to be dissipated poleward of the equator, it is quite clear from the alongshore evolution of the waves that at the lowest latitude of the latitude band of forcing (y_e), a proportion of the energy from the interior will remain. At y_e , the interior forcing has produced an anomaly η_e , concentrated on the slope, that acts as a source of variability for latitudes equatorward of y_e ; the dynamics equatorward of y_e are as discussed in section 4.

6. Application to western boundary sea level

Hong et al. (2000) and Minobe et al. (2017) have shown that western boundary sea level fluctuations can be described in terms of interior forcing with surprising skill using relatively simple models; for example, Hong et al. (2000) showed the first long Rossby wave generated by decadal period wind stress curl variability in the open ocean to contribute significantly to on-shelf variability along the U.S. East Coast. Aspects of this interior to coastal sea level relationship have been highlighted recently (see, e.g., Sallenger et al. 2012; Ezer et al. 2013; Thompson and Mitchum 2014; Higginson et al. 2015; Ezer 2017; Calafat et al. 2018). Despite this success, the physics remains less clear. The roles of topography and friction are often hidden in complex numerical models, statistical descriptions or idealizations. We consider the coastal effect of long period sea level change in the interior by considering $\omega \ll r/H$. In the steady state limit, the boundary adjustment is assumed to be fast relative to the variability in the interior; that is, following the initial propagating boundary wave adjustment, the interior sea level is represented at the boundary as a series of “arrested” waves, as in Csanady (1978)

(note that all imaginary parts of the solution become zero, and we are interested in the wave amplitudes).

Physically, for long period variability, friction acts as a sink in the conservation of potential vorticity relation. The effect of this in terms of sea level is made clearer by extending Csanady’s (1978) heat conduction analogy (to the β plane). Here, we write the vorticity relation Eq. (7) in terms of sea level in the form of an advection–diffusion equation:

$$-\frac{\partial}{\partial x} \left[\left(\frac{r}{f^2} \right) \frac{\partial \eta}{\partial x} \right] + \frac{\partial}{\partial y} \left(\frac{h}{f} \right) \frac{\partial \eta}{\partial x} - \frac{\partial}{\partial x} \left(\frac{h}{f} \right) \frac{\partial \eta}{\partial y} = 0, \quad (30)$$

where r/f^2 represents the analogous “diffusion” coefficient and h/f represents the analogous streamfunction of an “advecting velocity” (which is the Long Rossby wave speed if we multiply through by g). From this transport equation, we know that, in the limit of small friction, $r \rightarrow 0$ (first term vanishes), the conservation of potential vorticity must result in sea level contours following h/f contours. For nonzero r , the compensating effect of friction enables sea level contours to deviate from the h/f contours and “bend” toward a zonal orientation. This “bending” is more pronounced at lower latitudes where f is smaller (r/f^2 grows) but otherwise is not spatially uniform because the frictional compensation depends on how the flow interacts with the topography. For further discussion of this analogy, see Wise et al. (2018); for the transport streamfunction version, see Welander (1968) and Becker and Salmon (1997).

a. Influence of interior sea level

Western boundary sea level is related to interior sea level by

$$\eta(x, y) = \eta_{\text{in}}(y) - \sum_{j=1}^{\infty} \gamma_j C_j(x) \int_y^{y_p} \frac{d\eta_{\text{in}}}{ds} \left(\frac{y}{s} \right)^{\lambda_j} ds, \quad (31)$$

implying that boundary sea level is the interior sea level modified by a series of (arrested) waves. Steeper topography increases alongshore flow and increases the frictional compensation, bending the sea level contours zonally. Increasing the friction parameter also increases frictional compensation and widens the frictional boundary layer. In other words, there is an increased dissipation of energy at higher latitudes and a reduced equatorward flux of energy at lower latitudes relative to the westward flux of energy. This is represented by a reduction in magnitude of the second term in Eq. (31) (higher mode waves have been killed off), which implies that coastal sea level tends toward interior sea level at lower latitudes.

Integrating the second term of Eq. (31) by parts gives

$$\eta(x, y) = \sum_{j=1}^{\infty} \gamma_j C_j(x) \int_y^{y_p} \eta_{in}(s) \frac{d}{ds} \left[\left(\frac{y}{s} \right)^{\lambda_j} \right] ds, \quad (32)$$

where we have used $\sum_j \gamma_j C_j = -1$ (see appendix B). At $x = 0$, this relation describes sea level at the western boundary as a summation of weighted integrals of the interior sea level. The weighting function (the derivative part) acts to attenuate the interior sea level and displace it equatorward.

The coastal sea level for a vertical-sidewall boundary, found by Minobe et al. (2017) [second term in their Eq. (14)], can be written as

$$\eta(y) = - \int_y^{y_p} \eta_{in}(s) \frac{d}{ds} \left(\frac{y}{s} \right) ds. \quad (33)$$

Assuming that in the steep topography limit $\lambda_1 \rightarrow 1$ and $\lambda_j \gg 1$ for $j > 1$, then the first (arrested) wave mode of Eq. (32) differs from Eq. (33) only by a factor $\gamma_1 C_1(0)$; that is, if $\gamma_1 C_1(0) = -1$ they are equivalent. Note that Eq. (33) is also closely related to Eq. (9) in Hong et al. (2000); in that case the topographic effect, and indeed friction, are represented, implicitly, by tuning parameters (their α_N and α_S). In Fig. 11a we show the vertical-sidewall coastal sea level solution, the first-mode solution from Eq. (32) at $x = 0$, and the full solution of Eq. (32) at $x = 0$, in each case for the same interior sea level anomaly, which is representative of subtropical and subpolar gyres. The vertical-sidewall and mode-1 solutions differ by some factor, but the full solution shows a coastal sea level that has been displaced farther equatorward with greater attenuation. Consider now Fig. 11b, where we have significantly increased the friction parameter r . The solutions are now all equivalent, which implies that the vertical wall solution is the large-friction/small-topographic-width limit of Eq. (32). In practical terms this suggests that an open-ocean sea level anomaly, offshore of the North American east coast for example, will be felt at the coast with a reduced southward displacement and a reduced attenuation when the topography is steeper (e.g., a narrow shelf and upper slope).

b. Influence of interior and poleward sea level

From Eqs. (15) and (16), western boundary sea level is related to poleward sea level by

$$\eta(x, y) = \sum_{j=1}^{\infty} \alpha_j C_j(x) \left(\frac{y}{y_p} \right)^{\lambda_j}, \quad (34)$$

where the poleward sea level specifics are contained within α_j . Figure 12a shows sea level at the coast ($x = 0$) when sea level is imposed on the poleward boundary for two different shelf widths: 20 and 100 km, respectively,

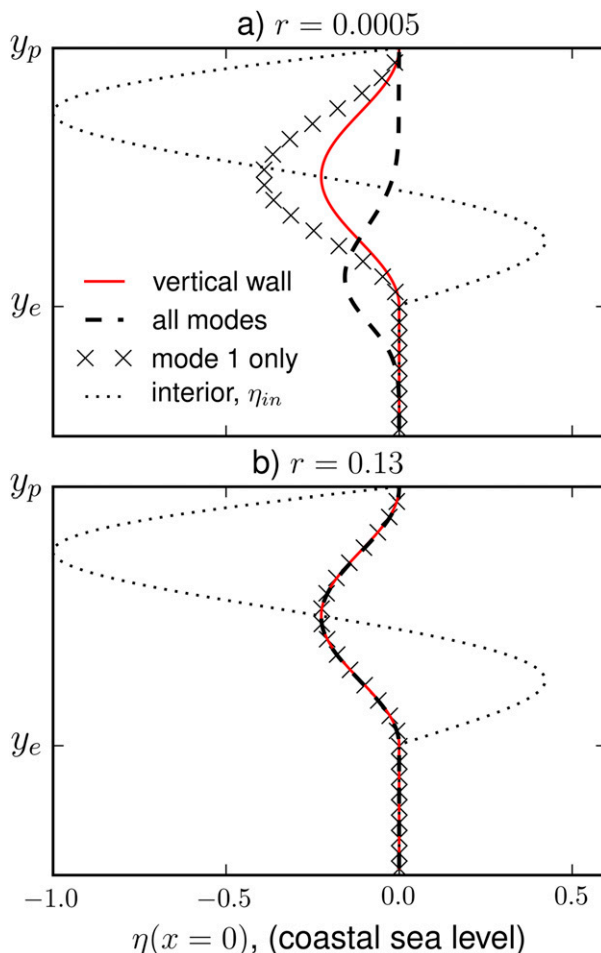


FIG. 11. Coastal sea level at the coast, $x = 0$, in response to an imposed interior sea level, η_{in} , that represents a double-gyre interior. The model including a shelf and slope (full solution and first wave mode only) is compared with the vertical-sidewall model for two friction coefficients: (a) $r = 0.0005$, (b) $r = 0.13$. Here y_p and y_e are 6000 and 2000 km poleward of the equator.

as well as for a larger friction parameter (with 100-km-width shelf). The imposed poleward boundary represents a sea level anomaly, poleward of the domain, which is negative on the shelf relative to the interior ocean. As expected from section 6a, Fig. 12a shows the negative sea level on the shelf has a reduced influence on lower latitude sea level when friction is increased or when the topography is steepened.

The above explanations are well demonstrated by looking at the combined effect of poleward Eq. (34) and interior sea level Eqs. (31) or (32) on coastal sea level using altimetry and tide gauge data along the U.S. East Coast. For the forcing data, we use a 22-yr mean (1993–2014 inclusive), AVISO altimeter-derived, mean dynamic sea level (MDSL) [i.e., sea level relative to the geoid—the “Ssalto/Duacs,” delayed mode, gridded

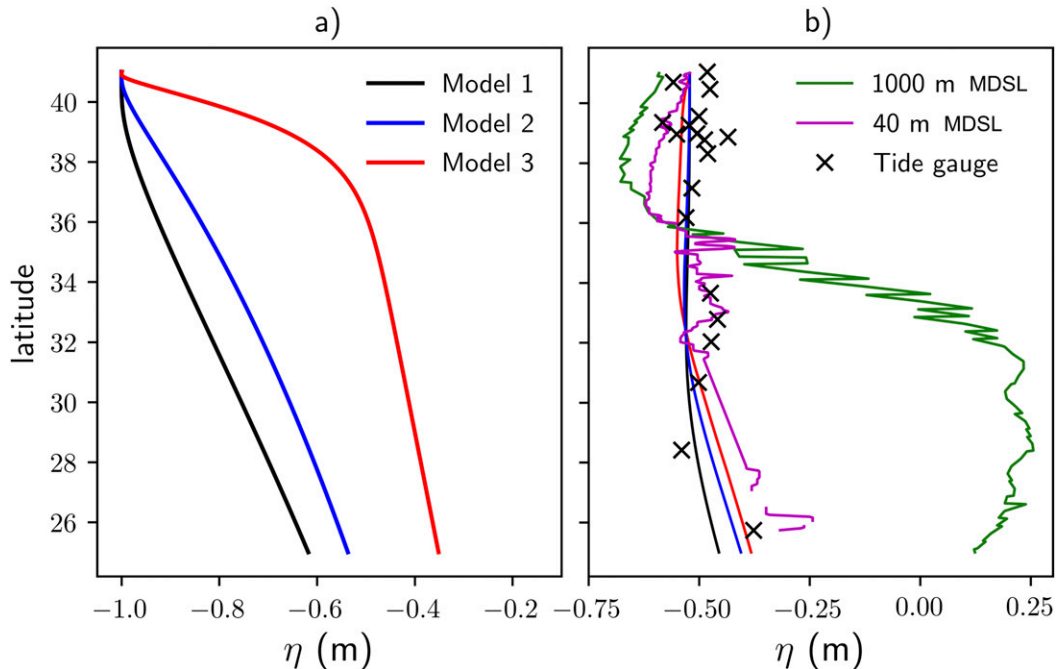


FIG. 12. (a) Modeled coastal sea level, $\eta(x = 0, y)$, when forced by a 1-m negative sea level anomaly on the shelf at 41° latitude (anomaly relative to the deep ocean, $\eta_{in} = 0$). Shelf geometry and friction control the equatorward propagation of information. The colors denote three model scenarios: black for shelf width 100 km and friction $r = 0.0005$, blue for shelf width 20 km and friction $r = 0.0005$, and red for shelf width 100 km and friction $r = 0.005$. Other parameters are as in Table 1. (b) Modeled coastal sea level, $\eta(x = 0, y)$, (black, blue, and red) along the U.S. East Coast when forced by altimetry-derived MDSL at the northern and offshore (green) boundaries. The model parameters are as in (a) but now with maximum depth of 1000 m and slope width 6766 m. MDSL along 40- and 1000-m depth contours are 22-yr means from altimetry (AVISO). Model and observations qualitatively agree.

absolute dynamic topography product using all available satellites—note that the satellite community refers to dynamic sea level as “dynamic topography,” although Gregory et al. (2019) recommend limiting this usage to refer to a calculation based on hydrographic density measurements]. To force the model we use this MDSL along the 1000-m depth contour between 41° and 25°N for our interior sea level, η_{in} , and the MDSL at 40 m, 41°N , for the poleward sea level (which is relaxed smoothly to the interior sea level). Figure 12b shows the model coastal sea level [$\eta(x = 0, y)$] relative to the altimetry MDSL along the 40-m depth contour and tide gauges. Mean dynamic topography at tide gauges is taken from Andersen et al. (2018), using the EIGEN-6C4 geoid (Förste et al. 2014) (note that the point values at tide gauges may show scatter because of limited knowledge of the geoid at small scales). The offset between tide gauge and satellite MDSL data is removed from the tide gauges by subtracting the absolute difference in the means of the 40 m MDSL and the tide gauges. The model compares well to observations. The southward increase in interior sea level across 36°N drives a smaller increase at lower latitudes along the Florida

coastline. This penetration may be experiencing an amplification as a result of the narrowing of the shelf along Florida, boosting the frictional compensation and bending sea level contours zonally, across h/f contours.

7. Conclusions

Waves at western boundaries are fundamental to how the ocean adjusts to changes in wind and buoyancy forcing. At low frequencies, we find that the β effect, friction, and bottom topography result in modified shelf waves and the appearance of a new class of leaky slope wave. Slope waves propagate along the continental slope and radiate damped short Rossby waves into the interior, and without friction are not trapped. Waves propagate alongshore typically at orders of $0.1\text{--}0.01\text{ m s}^{-1}$, and amplitudes decay over thousands of kilometers (shorter distances and slower for higher modes). The latitude dependence and parameter sensitivity of alongshore amplitude and phase make phase speed a potentially poor measure of information propagation.

The leaky slope waves are responsible for transmitting energy (information) as a jet along the slope and

eastward into the interior as damped short Rossby waves. This additional energy pathway due to the inclusion of the β effect is crucial to shortening the alongshore distance that the waves propagate. The waves decay alongshore (equatorward) as energy is dissipated at a rate that depends on latitude, the friction parameter and the bottom topography. As the friction parameter increases or the width of the shelf decreases, dissipation increases and the waves decay farther poleward. Pressure information resulting from high-latitude variability therefore propagates farther equatorward when the friction parameter is small and the shelf is wide. Conversely, interior variability penetrates onto the shelf to a greater extent (and at higher latitudes) when the friction parameter is large and the shelf is narrow. The limit of large friction is found to be equivalent to a vertical-sidewall boundary, where all but the first wave mode become negligible, implying that representing the bottom topography in this way maximizes high-latitude dissipation, minimizes the equatorward energy flux and maximizes penetration from the interior. These results follow naturally to long time period variability where the waves become arrested and represent the dynamic interior contribution to coastal sea level, which can be represented by a weighted integral of interior sea level values poleward of the target latitude, as in [Minobe et al. \(2017\)](#).

The simple model and analytic wave solutions provide a physical description for the adjustment process at western boundaries and the sensitivity of these waves to parameter configuration is a plausible explanation for some of the variation found between ocean circulation models in western boundary simulations. We note, however, that a number of important issues are not accounted for and should be considered for context.

First, a more sophisticated model involving stratification, mean flow and nonlinearities will modify the boundary response. For example, medium and strong stratification have been shown to induce a transition in shelf waves toward internal Kelvin waves ([Huthnance 1978](#)) and we expect that stratification effects become more important below the upper slope, complicating the response (e.g., [Huthnance 2004](#); [Kelly and Chapman 1988](#); [Chapman and Brink 1987](#)). First indications are that stratification can increase penetration ([Wise et al. 2018](#)), but more complete calculations are required to understand the effect in more realistic cases.

Another consideration is the western boundary mean flow. As discussed by [Mysak \(1980\)](#), a laterally sheared alongshore mean flow will modify the background potential vorticity, and waves (particularly short, slow waves), can be advected by the current and potentially amplified. Where the shear is comparable to f , a

divergence of sea level contours from h/f contours is expected.

There are also a number of ways to represent friction. One consideration is whether the friction parameter varies with depth, that is, whether $r = r(x)$. In that case the “advection–diffusion” transport equation [Eq. (30)] remains the same, implying that frictional compensation simply increases where r is larger. Other alternatives include nonlinear bottom friction or lateral friction. In these cases the frictional compensation takes on higher order forms and might amplify effects on the slope.

It is useful to make a few distinctions with respect to eastern boundaries. Unlike the radiation of short Rossby waves into the interior at western boundaries, [Clarke and Van Gorder \(1994\)](#) show that friction and topography (in a stratified model) allow low-frequency sea level signals to propagate poleward with decreasing amplitude, while the cross-shore sea level gradient is small at low latitudes and increases away from the coast at higher latitudes. Clearly friction and topography have an important influence at eastern boundaries, where information propagates along the boundary away from the equator, and into the ocean interior as long Rossby waves.

Topography and friction can be seen to modify the coastal sea level signals associated with waves at both eastern and western boundaries and accounting for these effects at the western boundary leads to some surprising results. Nonetheless, the western boundary waves can be interpreted as a means of propagating energy equatorward along the boundary, with part of that energy being dissipated by a combination of local friction and radiation of short Rossby waves into the interior.

Acknowledgments. This work has been supported by the Natural Environment Research Council (Anthony Wise: NE/L002469/1, EAO Doctoral Training Partnership; Chris W. Hughes: NE/K012789/1; and Jeff A. Polton: NE/L003325/1). The authors acknowledge the reviewers for their time and thoughtful comments and the AVISO Ssalto/Duacs altimeter products, produced and distributed by the Copernicus Marine and Environment Monitoring Service (CMEMS) (<http://www.marine.copernicus.eu>).

APPENDIX A

Solution Method

The solution method below draws upon the integral transform method for solving heat conduction problems detailed by [Özışık \(1993\)](#) applied to a problem with nonconstant coefficients, extending the approach of ([Do 1984](#); [Johnston and Do 1987](#); [Johnston 1994](#)).

Substituting $\tilde{\eta}(x, y, t) = \eta(x, y)e^{-i\omega t}$ into Eq. (7) yields

$$\frac{\partial^2 \eta}{\partial x^2} + b(x) \frac{\partial \eta}{\partial x} + f(y) a(x) \frac{\partial \eta}{\partial y} = 0, \quad \text{with} \quad (\text{A1})$$

$$a(x) = \frac{h'}{r - ih\omega}, \quad (\text{A2})$$

$$b(x) = \frac{h\beta - ih'\omega}{r - ih\omega}, \quad (\text{A3})$$

and $f(y) = \beta y$. This problem can alternatively be solved by first separating variables and solving the eigenvalue problem in x (via a number of methods). The method used below is particularly direct, obtaining the eigenvalues and eigenfunctions simultaneously, for a given frequency, from an explicitly defined matrix without finite differencing or special differentiation matrices. Other spectral methods (i.e., [Kaoullas and Johnson 2010](#)) may have greater efficiency and accuracy.

We first substitute $\eta(x, y) = \phi(x, y) + \eta_{\text{in}}(y)$ to make the boundary conditions at $x = 0$ and $x = x_{\text{in}}$ homogeneous, and Eq. (A1) becomes

$$\frac{\partial^2 \phi}{\partial x^2} + b(x) \frac{\partial \phi}{\partial x} + f(y) a(x) \frac{\partial \phi}{\partial y} + f(y) a(x) \frac{d\eta_{\text{in}}}{dy} = 0, \quad (\text{A4})$$

subject to $\partial\phi/\partial x \rightarrow 0$ at $x \rightarrow 0$, $\phi = 0$ at $x = x_{\text{in}}$, and $\phi = \eta_p(x) - \eta_{\text{in}}$ at $y = y_p$.

Defining an eigenvalue problem in Sturm–Liouville form consistent with the x boundary conditions,

$$\frac{d^2 \psi}{dx^2} + k^2 \psi(x) = 0, \quad (\text{A5})$$

subject to $d\psi/dx = 0$ at $x = 0$ and $\psi = 0$ at $x = x_{\text{in}}$. The eigenfunction solutions (in our case considered in the main text $\psi_j = \cos(k_j x)$, with $k_j = (j - 1/2)\pi/x_{\text{in}}$ for $j = 1, 2, \dots$) form a complete set of basis functions with the orthogonality condition

$$\int_0^{x_{\text{in}}} \psi_i(x) \psi_j(x) dx = \psi^N \delta_{ij}, \quad (\text{A6})$$

where δ_{ij} is the Kronecker delta ($\psi^N = x_{\text{in}}/2$ in our case). A function on $[0, x_{\text{in}}]$ satisfying the boundary conditions can be represented by

$$\phi(x, y) = \sum_j \widehat{\phi}_j(y) \psi_j(x) \quad \text{and} \quad (\text{A7})$$

$$\widehat{\phi}_j(y) = \frac{1}{\psi^N} \int_0^{x_{\text{in}}} \phi(x, y) \psi_j(x) dx. \quad (\text{A8})$$

Substituting Eq. (A7) into the second and third terms of Eq. (A4) gives

$$\begin{aligned} \frac{\partial^2 \phi}{\partial x^2} + b(x) \sum_{j=1}^{\infty} \frac{d\psi_j}{dx} \widehat{\phi}_j + f(y) a(x) \sum_{j=1}^{\infty} \psi_j \frac{d\widehat{\phi}_j}{dy} \\ + f(y) a(x) \frac{d\eta_{\text{in}}}{dy} = 0, \end{aligned} \quad (\text{A9})$$

and taking the transform of Eq. (A9) with respect to $\psi_i(x)$ (multiply through by ψ_i , integrate over x , and divide by ψ^N) yields a set of equations dependent on y only:

$$\frac{1}{\psi^N} \int_0^{x_{\text{in}}} a(x) \psi_i \sum_{j=1}^{\infty} \psi_j dx \frac{\partial \widehat{\phi}_j}{\partial y} + \left[-k_i^2 \delta_{ij} + \frac{1}{\psi^N} \int_0^{x_{\text{in}}} b(x) \psi_i \sum_{j=1}^{\infty} \frac{d\psi_j}{dx} dx \right] \frac{1}{f(y)} \widehat{\phi}_j = -\frac{1}{\psi^N} \int_0^{x_{\text{in}}} a(x) \psi_i dx \frac{d\eta_{\text{in}}}{dy}, \quad (\text{A10})$$

where we have made use of Green’s theorem (see [Özişik 1993](#), p. 526) to get

$$\frac{1}{\psi^N} \int_0^{x_{\text{in}}} \psi_i \frac{\partial^2 \phi}{\partial x^2} dx = -k_i^2 \widehat{\phi}_i. \quad (\text{A11})$$

Equation (A10) is more usefully written as a matrix equation

$$\mathbf{A} \frac{d\widehat{\boldsymbol{\phi}}}{dy} + \mathbf{B} \frac{1}{f(y)} \widehat{\boldsymbol{\phi}} = \mathbf{b} \frac{d\eta_{\text{in}}}{dy}, \quad (\text{A12})$$

where \mathbf{A} and \mathbf{B} are matrices and \mathbf{b} is a vector and where

$$A_{ij} = \frac{1}{\psi^N} \int_0^{x_{\text{in}}} a(x) \psi_i \psi_j dx, \quad (\text{A13})$$

$$B_{ij} = \text{diag}(-k_j^2) + \frac{1}{\psi^N} \int_0^{x_{\text{in}}} b(x) \psi_i \frac{d\psi_j}{dx} dx, \quad \text{and} \quad (\text{A14})$$

$$b_i = -\frac{1}{\psi^N} \int_0^{x_{\text{in}}} a(x) \psi_i dx, \quad (\text{A15})$$

with diag denoting a diagonal matrix. For matrices, the first subscript index denotes the row and the second denotes the column. The boundary condition for Eq. (A12) is

$$\widehat{\boldsymbol{\phi}}_p = \frac{1}{\psi^N} \int_0^{x_{\text{in}}} \psi_i [\eta_p(x) - \eta_{\text{in}}] dx, \quad (\text{A16})$$

and solving with the integrating factor

$$\mathbf{P}(y) = \exp \left[-\mathbf{T} \int_y^{y_p} \frac{1}{f(s)} ds \right], \quad (\text{A17})$$

where $\mathbf{T} = \mathbf{A}^{-1}\mathbf{B}$, gives the solution

$$\widehat{\boldsymbol{\phi}} = \mathbf{P}^{-1}\widehat{\boldsymbol{\phi}}_p - \mathbf{P}^{-1} \int_y^{y_p} \mathbf{P}(s) \frac{d\eta_{\text{in}}(s)}{ds} ds \mathbf{A}^{-1}\mathbf{b}. \quad (\text{A18})$$

We recover ϕ by substituting Eq. (A18) into Eq. (A7) and recover η by adding η_{in} , giving

$$\eta(x, y) = \eta_{\text{in}} + \boldsymbol{\psi} \cdot \left[\mathbf{P}^{-1}\widehat{\boldsymbol{\phi}}_p - \mathbf{P}^{-1} \int_y^{y_p} \mathbf{P}(s) \frac{d\eta_{\text{in}}(s)}{ds} ds \mathbf{A}^{-1}\mathbf{b} \right], \quad (\text{A19})$$

where $\boldsymbol{\psi} = [\psi_1, \psi_2, \dots]$. The solution can be written as a series. For a diagonalizable \mathbf{T} , we have the eigen-decomposition $\mathbf{T} = \mathbf{Q}\boldsymbol{\Lambda}\mathbf{Q}^{-1}$, where $\boldsymbol{\Lambda}$ is diagonal with each element λ_j being an eigenvalue of \mathbf{T} and the columns \mathbf{q}_j of \mathbf{Q} being the corresponding eigenvectors of \mathbf{T} . Then using the identity $\exp(\mathbf{T}) = \exp(\mathbf{Q}\boldsymbol{\Lambda}\mathbf{Q}^{-1}) = \mathbf{Q} \text{diag}(e^{\lambda_j}) \mathbf{Q}^{-1}$ and ordering the terms in the series by λ_j , the solution is

$$\eta(x, y) = \eta_{\text{in}}(y) - \sum_{j=1}^{\infty} \gamma_j C_j(x) A_j^{\text{in}}(y) + \sum_{j=1}^{\infty} \alpha_j C_j(x) A_j^p(y), \quad (\text{A20})$$

$$C_j(x) = \boldsymbol{\psi}(x) \cdot \mathbf{q}_j, \quad (\text{A21})$$

$$A_j^{\text{in}}(y) = \exp \left[-\lambda_j \int_y^{y_p} 1/f(s) ds \right] \times \int_y^{y_p} \frac{d\eta_{\text{in}}}{ds} \exp \left[\lambda_j \int_s^{y_p} 1/f(\hat{s}) d\hat{s} \right] ds, \quad \text{and} \quad (\text{A22})$$

$$A_j^p(y) = \exp \left[-\lambda_j \int_y^{y_p} 1/f(s) ds \right], \quad (\text{A23})$$

where $\gamma_j = (\mathbf{Q}^{-1}\mathbf{A}^{-1}\mathbf{b})_j$ and $\alpha_j = (\mathbf{Q}^{-1}\widehat{\boldsymbol{\phi}}_p)_j$ are constants and s and \hat{s} are dummy integration variables.

APPENDIX B

Weighted Integral of Interior Sea Level Formulation

Left multiplying Eq. (A12) by $\boldsymbol{\psi} \cdot \mathbf{A}^{-1}$ gives

$$\boldsymbol{\psi} \cdot \frac{d\widehat{\boldsymbol{\phi}}}{dy} + \boldsymbol{\psi} \cdot \mathbf{A}^{-1}\mathbf{B} \frac{1}{f(y)} \widehat{\boldsymbol{\phi}} = \boldsymbol{\psi} \cdot \mathbf{A}^{-1}\mathbf{b} \frac{d\eta_{\text{in}}}{dy}. \quad (\text{B1})$$

Dividing Eq. (A9) through by $f(y)a(x)$ gives an expression for $\boldsymbol{\psi} \cdot d\widehat{\boldsymbol{\phi}}/dy$ into which substituting Eq. (B1) gives

$$\begin{aligned} & \frac{1}{f(y)a(x)} \left[\frac{\partial^2 \phi}{\partial x^2} + b(x) \sum_{j=1}^{\infty} \frac{d\psi_j}{dx} \widehat{\phi}_j \right] + \frac{d\eta_{\text{in}}}{dy} \\ & = \boldsymbol{\psi} \cdot \mathbf{A}^{-1}\mathbf{B} \frac{1}{f(y)} \widehat{\boldsymbol{\phi}} - \boldsymbol{\psi} \cdot \mathbf{A}^{-1}\mathbf{b} \frac{d\eta_{\text{in}}}{dy}. \end{aligned} \quad (\text{B2})$$

If at $y = y_p$ we take ϕ to be zero, then $\widehat{\phi}_j$ are also zero and the first terms on both sides of Eq. (B2) become zero. This result implies that $\boldsymbol{\psi} \cdot \mathbf{A}^{-1}\mathbf{b} = -1$. Last, we have

$$\sum_j \gamma_j C_j = \boldsymbol{\psi} \cdot \mathbf{Q}\mathbf{Q}^{-1}\mathbf{A}^{-1}\mathbf{b} = \boldsymbol{\psi} \cdot \mathbf{A}^{-1}\mathbf{b} = -1. \quad (\text{B3})$$

REFERENCES

- Allen, J., and R. Romea, 1980: On coastal trapped waves at low latitudes in a stratified ocean. *J. Fluid Mech.*, **98**, 555–585, <https://doi.org/10.1017/S0022112080000286>.
- Andersen, O. B., and Coauthors, 2018: Improving the coastal mean dynamic topography by geodetic combination of tide gauge and satellite altimetry. *Mar. Geod.*, **41**, 517–545, <https://doi.org/10.1080/01490419.2018.1530320>.
- Becker, J. M., and R. Salmon, 1997: Eddy formation on a continental slope. *J. Mar. Res.*, **55**, 181–200, <https://doi.org/10.1357/0022240973224418>.
- Brink, K. H., and J. Allen, 1978: On the effect of bottom friction on barotropic motion over the continental shelf. *J. Phys. Oceanogr.*, **8**, 919–922, [https://doi.org/10.1175/1520-0485\(1978\)008<0919:OTEOBF>2.0.CO;2](https://doi.org/10.1175/1520-0485(1978)008<0919:OTEOBF>2.0.CO;2).
- Bryan, F. O., M. W. Hecht, and R. D. Smith, 2007: Resolution convergence and sensitivity studies with North Atlantic circulation models. Part I: The Western Boundary Current System. *Ocean Modell.*, **16**, 141–159, <https://doi.org/10.1016/j.ocemod.2006.08.005>.
- Buchwald, V., and J. Adams, 1968: The propagation of continental shelf waves. *Proc. Roy. Soc. London*, **305**, 235–250, <https://doi.org/10.1098/rspa.1968.0115>.
- Buckley, M. W., and J. Marshall, 2016: Observations, inferences, and mechanisms of the Atlantic meridional overturning circulation: A review. *Rev. Geophys.*, **54**, 5–63, <https://doi.org/10.1002/2015RG000493>.
- Calafat, F. M., T. Wahl, F. Lindsten, J. Williams, and E. Frajka-Williams, 2018: Coherent modulation of the sea-level annual cycle in the United States by Atlantic Rossby waves. *Nat. Commun.*, **9**, 2571, <https://doi.org/10.1038/s41467-018-04898-y>.
- Chapman, D. C., and K. H. Brink, 1987: Shelf and slope circulation induced by fluctuating offshore forcing. *J. Geophys. Res.*, **92**, 11 741–11 759, <https://doi.org/10.1029/JC092iC11p11741>.
- Clarke, A. J., and C. Shi, 1991: Critical frequencies at ocean boundaries. *J. Geophys. Res.*, **96**, 10 731–10 738, <https://doi.org/10.1029/91JC00933>.
- , and S. Van Gorder, 1994: On ENSO coastal currents and sea levels. *J. Phys. Oceanogr.*, **24**, 661–680, [https://doi.org/10.1175/1520-0485\(1994\)024<0661:OECCAS>2.0.CO;2](https://doi.org/10.1175/1520-0485(1994)024<0661:OECCAS>2.0.CO;2).
- Csanady, G. T., 1978: The arrested topographic wave. *J. Phys. Oceanogr.*, **8**, 47–62, [https://doi.org/10.1175/1520-0485\(1978\)008<0047:TATW>2.0.CO;2](https://doi.org/10.1175/1520-0485(1978)008<0047:TATW>2.0.CO;2).
- Deremble, B., E. Johnson, and W. Dewar, 2017: A coupled model of interior balanced and boundary flow. *Ocean Modell.*, **119**, 1–12, <https://doi.org/10.1016/j.ocemod.2017.09.003>.

- Do, D., 1984: A method for solving diffusion and reaction problems with nonuniform activity catalysts. *Chem. Eng. Sci.*, **39**, 1519–1522, [https://doi.org/10.1016/0009-2509\(84\)80011-1](https://doi.org/10.1016/0009-2509(84)80011-1).
- Ezer, T., 2017: A modeling study of the role that bottom topography plays in gulf stream dynamics and in influencing the tilt of mean sea level along the US East Coast. *Ocean Dyn.*, **67**, 651–664, <https://doi.org/10.1007/s10236-017-1052-5>.
- , L. P. Atkinson, W. B. Corlett, and J. L. Blanco, 2013: Gulf Stream's induced sea level rise and variability along the US mid-Atlantic coast. *J. Geophys. Res. Oceans*, **118**, 685–697, <https://doi.org/10.1002/jgrc.20091>.
- Förste, C., and Coauthors, 2014: EIGEN-6C4 the latest combined global gravity field model including GOCE data up to degree and order 2190 of GFZ Potsdam and GRGS Toulouse. GFZ Data Services, <https://doi.org/10.5880/icgem.2015.1>.
- Gill, A., and E. Schumann, 1974: The generation of long shelf waves by the wind. *J. Phys. Oceanogr.*, **4**, 83–90, [https://doi.org/10.1175/1520-0485\(1974\)004<0083:TGOLSW>2.0.CO;2](https://doi.org/10.1175/1520-0485(1974)004<0083:TGOLSW>2.0.CO;2).
- Gregory, J. M., and Coauthors, 2019: Concepts and terminology for sea level: Mean, variability and change, both local and global. *Surv. Geophys.*, **40**, 1251–1289, <https://doi.org/10.1007/S10712-019-09525-z>.
- Higginson, S., K. R. Thompson, P. L. Woodworth, and C. W. Hughes, 2015: The tilt of mean sea level along the east coast of North America. *Geophys. Res. Lett.*, **42**, 1471–1479, <https://doi.org/10.1002/2015GL063186>.
- Hong, B., W. Sturges, and A. J. Clarke, 2000: Sea level on the U.S. East Coast: Decadal variability caused by open ocean wind-curl forcing. *J. Phys. Oceanogr.*, **30**, 2088–2098, [https://doi.org/10.1175/1520-0485\(2000\)030<2088:SLOTUS>2.0.CO;2](https://doi.org/10.1175/1520-0485(2000)030<2088:SLOTUS>2.0.CO;2).
- Hughes, C. W., and M. P. Meredith, 2006: Coherent sea-level fluctuations along the global continental slope. *Philos. Trans. Roy. Soc. London*, **364A**, 885–901, <https://doi.org/10.1098/rsta.2006.1744>.
- , I. Fukumori, S. M. Griffies, J. M. Huthnance, S. Minobe, P. Spence, K. R. Thompson, and A. Wise, 2019: Sea level and the role of coastal trapped waves in mediating the influence of the open ocean on the coast. *Surv. Geophys.*, **40**, 1467–1492, <https://doi.org/10.1007/S10712-019-09535-X>.
- Huthnance, J. M., 1975: On trapped waves over a continental shelf. *J. Fluid Mech.*, **69**, 689–704, <https://doi.org/10.1017/S0022112075001632>.
- , 1978: On coastal trapped waves: Analysis and numerical calculation by inverse iteration. *J. Phys. Oceanogr.*, **8**, 74–92, [https://doi.org/10.1175/1520-0485\(1978\)008<0074:OCTWAA>2.0.CO;2](https://doi.org/10.1175/1520-0485(1978)008<0074:OCTWAA>2.0.CO;2).
- , 1987: Along-shelf evolution and sea levels across the continental slope. *Cont. Shelf Res.*, **7**, 957–974, [https://doi.org/10.1016/0278-4343\(87\)90008-2](https://doi.org/10.1016/0278-4343(87)90008-2).
- , 2004: Ocean-to-shelf signal transmission: A parameter study. *J. Geophys. Res.*, **109**, C12029, <https://doi.org/10.1029/2004JC002358>.
- Huthnance, J., L. Mysak, and D.-P. Wang, 1986: Coastal trapped waves. *Baroclinic Processes on Continental Shelves*, C. N. K. Mooers, Coastal and Estuarine Sciences Series, Vol. 3, Amer. Geophys. Union, 1–18.
- Johnson, H. L., and D. P. Marshall, 2002: A theory for the surface Atlantic response to thermohaline variability. *J. Phys. Oceanogr.*, **32**, 1121–1132, [https://doi.org/10.1175/1520-0485\(2002\)032<1121:ATFTSA>2.0.CO;2](https://doi.org/10.1175/1520-0485(2002)032<1121:ATFTSA>2.0.CO;2).
- Johnston, P., 1994: A solution method for the Graetz problem for non-Newtonian fluids with Dirichlet and Neumann boundary conditions. *Math. Comput. Modell.*, **19**, 1–19, [https://doi.org/10.1016/0895-7177\(94\)90045-0](https://doi.org/10.1016/0895-7177(94)90045-0).
- , and D. Do, 1987: A new method for solving a large class of heat and mass transfer problems. *Chem. Eng. Commun.*, **49**, 247–271, <https://doi.org/10.1080/00986448708911806>.
- Kanzow, T., H. Johnson, D. Marshall, S. Cunningham, J.-M. Hirschi, A. Mujahid, H. Bryden, and W. Johns, 2009: Basinwide integrated volume transports in an eddy-filled ocean. *J. Phys. Oceanogr.*, **39**, 3091–3110, <https://doi.org/10.1175/2009JPO4185.1>.
- Kaoullas, G., and E. Johnson, 2010: Fast accurate computation of shelf waves for arbitrary depth profiles. *Cont. Shelf Res.*, **30**, 833–836, <https://doi.org/10.1016/j.csr.2009.12.010>.
- Kelly, K. A., and D. C. Chapman, 1988: The response of stratified shelf and slope waters to steady offshore forcing. *J. Phys. Oceanogr.*, **18**, 906–925, [https://doi.org/10.1175/1520-0485\(1988\)018<0906:TROSSA>2.0.CO;2](https://doi.org/10.1175/1520-0485(1988)018<0906:TROSSA>2.0.CO;2).
- Longuet-Higgins, M. S., 1964: On group velocity and energy flux in planetary wave motions. *Deep-Sea Res. Oceanogr. Abstr.*, **11**, 35–42, [https://doi.org/10.1016/0011-7471\(64\)91080-0](https://doi.org/10.1016/0011-7471(64)91080-0).
- Marshall, D. P., and H. L. Johnson, 2013: Propagation of meridional circulation anomalies along western and eastern boundaries. *J. Phys. Oceanogr.*, **43**, 2699–2717, <https://doi.org/10.1175/JPO-D-13-0134.1>.
- Miles, J. W., 1972: Kelvin waves on oceanic boundaries. *J. Fluid Mech.*, **55**, 113–127, <https://doi.org/10.1017/S0022112072001685>.
- Minobe, S., M. Terada, B. Qiu, and N. Schneider, 2017: Western boundary sea level: A theory, rule of thumb, and application to climate models. *J. Phys. Oceanogr.*, **47**, 957–977, <https://doi.org/10.1175/JPO-D-16-0144.1>.
- Moore, D. W., 1968: Planetary-gravity waves in an equatorial ocean. Ph.D. dissertation, Harvard University, 207 pp.
- Mysak, L. A., 1980: Topographically trapped waves. *Annu. Rev. Fluid Mech.*, **12**, 45–76, <https://doi.org/10.1146/annurev.fl.12.010180.000401>.
- Özişik, M. N., 1993: *Heat Conduction*. 2nd ed. John Wiley and Sons, 692 pp.
- Robinson, A., 1964: Continental shelf waves and the response of sea level to weather systems. *J. Geophys. Res.*, **69**, 367–368, <https://doi.org/10.1029/JZ069i002p00367>.
- Roussenov, V. M., R. G. Williams, C. W. Hughes, and R. J. Bingham, 2008: Boundary wave communication of bottom pressure and overturning changes for the North Atlantic. *J. Geophys. Res.*, **113**, C08042, <https://doi.org/10.1029/2007JC004501>.
- Sallenger, A. H., Jr., K. S. Doran, and P. A. Howd, 2012: Hotspot of accelerated sea-level rise on the Atlantic coast of North America. *Nat. Climate Change*, **2**, 884–888, <https://doi.org/10.1038/nclimate1597>.
- Salmon, R., 1998: *Lectures on Geophysical Fluid Dynamics*. Oxford University Press, 400 pp.
- Thompson, P., and G. Mitchum, 2014: Coherent sea level variability on the North Atlantic western boundary. *J. Geophys. Res. Oceans*, **119**, 5676–5689, <https://doi.org/10.1002/2014JC009999>.
- Wajsowicz, R. C., and A. Gill, 1986: Adjustment of the ocean under buoyancy forces. Part I: The role of Kelvin waves. *J. Phys. Oceanogr.*, **16**, 2097–2114, [https://doi.org/10.1175/1520-0485\(1986\)016<2097:AOTOUB>2.0.CO;2](https://doi.org/10.1175/1520-0485(1986)016<2097:AOTOUB>2.0.CO;2).
- Welander, P., 1968: Wind-driven circulation in one- and two-layer oceans of variable depth. *Tellus*, **20**, 1–16, <https://doi.org/10.1111/j.2153-3490.1968.tb00347.x>.
- Wise, A., C. W. Hughes, and J. A. Polton, 2018: Bathymetric influence on the coastal sea level response to ocean gyres at western boundaries. *J. Phys. Oceanogr.*, **48**, 2949–2964, <https://doi.org/10.1175/JPO-D-18-0007.1>.
- Zhai, X., H. L. Johnson, and D. P. Marshall, 2010: Significant sink of ocean-eddy energy near western boundaries. *Nat. Geosci.*, **3**, 608–612, <https://doi.org/10.1038/ngeo943>.